Università "Federico II" di Napoli

Dottorato di Ricerca in "Rischio Sismico"

XVII Ciclo - 2005

An Interferometric seismic sensor:

theoretical model and experimental performances

Dott. Fausto Acernese

Università "Federico II" di Napoli

Dottorato di Ricerca in "Rischio Sismico"

XVII Ciclo - 2005

An Interferometric seismic sensor:

theoretical model and experimental performances

Dott. Fausto Acernese

Thesis Commitee

Prof. Paolo Gasparini (Ph.D. coordinator)

Prof. Leopoldo Milano (Advisor)

Dr.ssa Rosa di Maio (Advisor)

Reviewers

Prof. Luca Crescentini

Prof. Mauro Dolce

Prof. Francesco Silvestri

Ai miei genitori,

perché senza di loro nulla sarebbe stato possible.

Contents

Introduction

Seismic Hazard describes the potential for dangerous, earthquake-related natural phenomena such as ground shaking, fault rupture, or soil liquefaction. These phenomena could cause adverse consequences to society such as the destruction of buildings of the loss of life. *Seismic Risk* is the probability of occurrence of these consequences.

The output of the seismic hazard analysis could be a description of the intensity of shaking of a nearby magnitude eight earthquake or a map which shows levels of ground shaking in different regions of a country having equal chance of being exceeded, The output of the seismic risk analysis could be the probability of damage from a nearby magnitude eight earthquake or the probability of fatalities due to seismically induced buildings accidents.

For a correct evaluation of the seismic hazard we have to consider several aspects:

- the characterization of the source or sources of the hazard, in terms of size, spatial location, orientation, slip type, probability of rupture, etc.;

- the characterization of the seismic wave propagation until a particular location;

- the site response to a particular earthquake, in terms of peak ground acceleration (PGA) or in term of response spectra (relation between amplitude of the ground accelerations and its frequency): in fact the amplitude of earthquake ground motion can be increased or decreased by both the properties and the

configuration of the near surface material through which seismic waves propagate. For this reason the same earthquake, at the same distance from the source, can produce different ground acceleration in function of the site response.

Consider the approach to seismic zonation of a country, characterized by ground motion, slope instability and liquefaction, we can divide the knowledge level in three parts which are more and more accurate:

Grade 1: the only knowledge we have is from historical earthquakes, from interviews with local residents and from geological and geomorphological maps; the typical scale of this mapping is $1 : 1000000 \div 1 : 50000$.

Grade 2: the knowledge is from simplified geotechnical studies, from air photos, from field studies and from remote sensing; the typical scale of this mapping is $1 : 100000 \div 1 : 10000$.

Grade 3: this level of knowledge is the more accurate and it is based on geotechnical investigation and analysis of recorded data of ground motion; ; the typical scale of this mapping is $1 : 25000 \div 1 : 1 : 5000$.

It is clear that for a more accurate mapping of seismic hazard it is necessary to have a kind of sensors which can record with high accuracy and in a broad frequency band, in particular at low frequency, because much of the energy released during an earthquake results in teleseismic signals with periods ranging from hours to seconds.

The work we present is related to the development of a new kind of seismic sensor based on the inteferometric phenomena of light. The laser interferometry is one of the most sensitive and widely used techniques for small displacement measurement, whose success is mainly due to its very good performances and the large availability, high quality and relatively low cost of optical components and laser sources. This

technique is flexible enough to be effectively used in very different applications, like the one we present in this work. This work is organized in the following parts:

- in the chapter 1 we will discuss some hints about seismic signals and about the instruments used to measure them.

- in the chapter 2 we will discuss about the interferometric phenomena of light and we will show the theoretical analysis of possible instrument based on an interferometric device;

- in the chapter 3 the experimental results obtained with a prototype developed will be shown;

- in the chapter 4 we will present the theoretical model and some preliminary results about another kind of interferometric seismic sensor based on feedback principle and we will discuss how to improve its characteristics.

Chapter 1

Hints about seismic waves propagation and measurement

Any quantitative description of seismic waves requires the ability to characterize the internal forces and deformations in solid materials. We now begin a brief review of theory of stress and strain, which do not exist independently in a material; they are linked through the constitutive relationship that describes the nature of elastic solids. Then, using the stress and strain theory we construct the seismic wave equation for elastic wave propagation in uniform whole space. Solving this equation, we obtain that the solutions are plane waves called *body waves*. However, when a free surface exists in a medium, other solutions are possible, which are called *surface waves*. At the end of the chapter we present a review about the actual seismic instruments, in particular mechanical and electromagnetic seismometers.

1.1 Stress and Strain

1.1.1 Stress tensor

A stress tensor describes internal forces in a solid volume. Consider a small volume from the interior of a solid body. What external forces act on this block? There are "body forces", originated outside the block and which act on every molecule within the block. There are also "surface forces", which are forces that act on the surface of the block through surrounding molecules, through atomic and molecular bonding. These forces are primarily between neighbors and next-nearest neighbors. The surface force per unit area of the surface is called the stress [1].

Consider an infinitesimal plane of arbitrary orientation within a homogeneous elastic medium in static equilibrium. The orientation of the plane can be specified by its unit normal vector $\hat{n}$. The force per unit of area exerted by the side in the directional of $\hat{n}$ across this plane is termed traction and is represented by a vector $\mathbf{t}(\hat{n})$. The $\mathbf{t}$ component which is normal to the plane is termed the normal stress; the parallel component is called the shear stress. In the case of fluid, there are no shear stress and $\mathbf{t} = -P\hat{n}$, where P is the pressure.

The stress tensor τ_{ij} in Cartesian coordinates system may be defined by the traction across the x_1x_2, x_2x_3 and x_1x_3 planes, with normals n_3, n_1 and n_2 respectively, as:

$$\tau_{ij} = \begin{bmatrix} t_1(n_1) & t_1(n_2) & t_1(n_3) \\ t_2(n_1) & t_2(n_2) & t_2(n_3) \\ t_3(n_1) & t_3(n_2) & t_3(n_3) \end{bmatrix} \tag{1.1}$$

The stress tensor is symmetric and so contains only six independent components.

The traction across any arbitrary plane of orientation defined by $\hat{n}$ may be obtained by multiplying the stress tensor by $\hat{n}$, that is

$$\mathbf{t}(\hat{n}) = \tau\hat{\mathbf{n}} \tag{1.2}$$

The stress tensor is simply a linear operator which produces the traction vector **t** from normal vector **n**, and, in this sense, the stress tensor exists independently of any particular coordinate system. The stress tensor generally varies with position in a material; it is a measure of the force acting on infinitesimal planes at each point in the solid. Stress provides a measure only of the forces exerted across these planes and has units of force per unit of area. However, other forces may be present (for example the gravity); these forces are termed body forces and have unit of forces per unit volume or mass.

1.1.2   Strain tensor

Consider a volume in three dimensional space, any point can be identified by a vector $\mathbf{r} = (x_1, x_2, x_3)$. If there is a deformation, the same point can be indicated with a new vector $\mathbf{r}' = (x'_1, x'_2, x'_3)$, and we define the deformation vector $\mathbf{u} = \mathbf{r}' - \mathbf{r}$. The coordinates x'_i depend on the coordinates x_i and so also the deformations u_i depend on x_i. Consider an infinitesimal deformation, the differential $d\mathbf{u}$ is[1]

$$du_i = \partial_j u_{ij} dx_j + O(dx_j^2) \tag{1.3}$$

The matrix $\partial_j u_{ij}$ is the Jacobian matrix J (displacement gradient matrix) associated with the displacement field $\mathbf{u}$ in the Cartesian coordinate system $\mathbf{x}$.

The matrix J can be written as a sum of a symmetric matrix $\hat{\epsilon}$ and a skew-symmetric matrix $\hat{\omega}$, where $\hat{\epsilon} = (J + J^T)/2$ and $\hat{\omega} = (J - J^T)/2$. The elements of $\hat{\epsilon}$ and $\hat{\omega}$ are

$$
\begin{aligned}
\epsilon_{ij} &= \frac{1}{2} \left(\partial_j u_{ij} + \partial_i u_{ji} \right) \\
\omega_{ij} &= \frac{1}{2} \left(\partial_j u_{ij} - \partial_i u_{ji} \right)
\end{aligned}
\tag{1.4}
$$

---

[1]We adopt the Einstein's convention that repeated index means the sum over this index and the convention that $\partial_j u_{ij} = \frac{\partial u_i}{\partial x_j}$ and $\dot{a} = \frac{da}{dt}$.

The symmetric matrix $\hat{\epsilon}$ represents a second order symmetric tensor (the irrotational strain sensor) and $\hat{\omega}$ a second order skew-symmetric rotation matrix [1].

The effect of $\hat{\epsilon}$ and $\hat{\omega}$ may be illustrated by considering what happens to an infinitesimal cube (see figure 1.1). The off-diagonal elements of $\hat{\epsilon}$ cause shear strain; for example, in two dimension, if $\hat{\omega} = 0$ and there is no volume change, then

$$J = \hat{\epsilon} = \begin{bmatrix} 0 & \theta \\ \theta & 0 \end{bmatrix} = \begin{bmatrix} 0 & \partial_3 u_{13} \\ \partial_1 u_{31} & 0 \end{bmatrix} \tag{1.5}$$

where θ is the angle in radians through which each side rotates. Note that the total change in angle between the sides is 2θ. In contrast, the $\hat{\omega}$ tensor causes rigid rotation, for example, if $\hat{\epsilon} = 0$, then

$$J = \hat{\omega} = \begin{bmatrix} 0 & \theta \\ -\theta & 0 \end{bmatrix} = \begin{bmatrix} 0 & \partial_3 u_{13} \\ \partial_1 u_{31} & 0 \end{bmatrix} \tag{1.6}$$
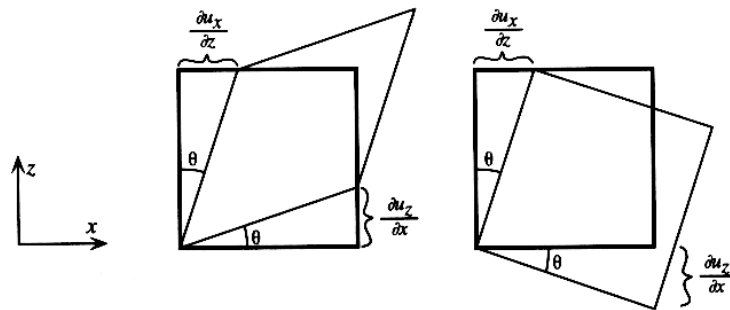

Figure 1.1: The different effects of the strain tensor $\hat{\epsilon}$ (on the left) and the rotation sensor $\hat{\omega}$ (on the right) are illustrated by the deformation of a square in the xz plane in a Cartesian reference system x, y, z.

1.1.3   The linear stress-strain relationship

Stress and strain are linked in elastic media by a stress-strain relationship or constitutive relationship. The most general linear relationship between stress and strain

tensor is the Hooke's law [1]:

$$\tau_{ij} = c_{ijkl}\epsilon_{kl} \tag{1.7}$$

where c_{ijkl} is termed the elastic tensor. The equation 1.7 assumes perfect elasticity: there is no energy loss as the material deforms in response to applied stress. The elastic tensor is a fourth-order tensor with 81 components. However, because of the symmetry of the stress and strain tensor, only 21 of these components are independent.

If we assume isotropy (c_{ijkl} is invariant with respect to rotation), it can be shown that the number of independent parameters can be reduced to two and

$$c_{ijkl} = \lambda\delta_{ij} + \mu(\delta_{il}\delta_{jk} + \delta_{ik}\delta_{jl}) \tag{1.8}$$

where λ and μ are called Lamé parameters of the material and δ_{ij} is the Kronecker delta. Then the stress-strain relationship 1.7 for an isotropic solid is [2]:

$$\begin{aligned}\tau_{ij} &= [\lambda\delta_{ij} + \mu(\delta_{il}\delta_{jk} + \delta_{ik}\delta_{jl})]\epsilon_{kl} \\ &= \lambda\delta_{ij}\epsilon_{kk} + 2\mu\epsilon_{ij}\end{aligned} \tag{1.9}$$

The two Lamé parameters completely describe the linear stress-strain relationship within an isotropic solid: μ is termed the shear modulus and it is a measure of the resistance of the material to shearing; λ does not have a simple physical explanation. Other commonly used elastic constants for describing isotropic solids are:

- the Young modulus E: the ratio of extensional stress to the resulting extensional strain for a cylinder being pulled on both ends;

$$E = \frac{(3\lambda + 2\mu)\mu}{(\lambda + \mu)}$$

- the bulk modulus k: the ratio of hydrostatic pressure to the resulting volume change, a measure of the incompressibility of the material;

$$k = \frac{\lambda + 2\mu}{3}$$

- the Poisson's ration σ: the ratio of the lateral contraction of a cylinder (being pulled on its ends) to its longitudinal extension.

$$\sigma = \frac{\lambda}{2(\lambda + mu)}$$

1.2 The seismic wave equation

1.2.1 The momentum equation

In the section 1.1 the stress, strain and displacement field are considered in static equilibrium and unchanging with time. However, because seismic waves are time-dependent phenomena that involve velocities and accelerations, we need to account for the effect of momentum. We do this by applying Newton's law to a continuous medium.

Consider the force on an infinitesimal cube $dV = dx_1 dx_2 dx_3$ in (x_1, x_2, x_3) coordinate system, as shown in figure 1.2. The surface forces on each surface of the cube are given by the product of the traction vector and the surface area:

$$F_i^S = \tau_{ij} \hat{n}_j \tag{1.10}$$

and, integrating over all the face

$$F^S = \int_S \tau \cdot \hat{\mathbf{n}} dS \tag{1.11}$$

There may also exist a net body force on the cube that acts proportionally to the volume of material, that, for all the volume, is

$$F^{body} = \int_V \mathbf{f} dV \tag{1.12}$$

The mass of out infinitesimal cube is $dm = \rho dV$, where ρ is the density. The acceleration of the cube is given by the second time derivative of the displacement $\mathbf{u}$.
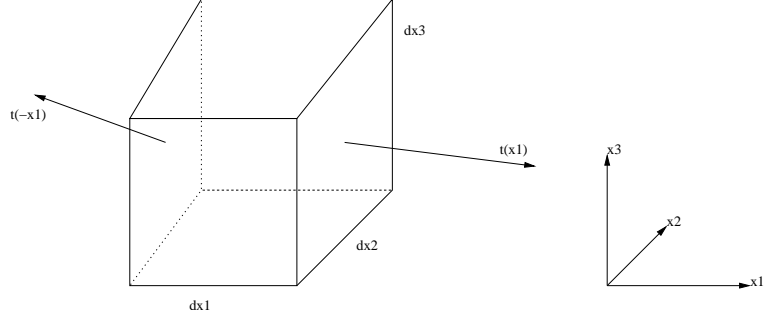
Figure 1.2: Pictures of the force on the (x_2, x_3) face of an infinitesimal cube in (x_1, x_2, x_3) Cartesian space.

Substituting the equation 1.11 and 1.12 into $\mathbf{F} = m\mathbf{a}$ we obtain

$$\int_S \tau \cdot \hat{\mathbf{n}} dS + \int_V \mathbf{f} dV = \rho \ddot{\mathbf{u}} \tag{1.13}$$

By the divergence theorem applied to tensor

$$\int_S \tau \hat{\mathbf{n}} dS = \int_V \nabla \cdot \tau dV \tag{1.14}$$

then the equation 1.13 becomes

$$\int_V \left[\nabla \cdot \tau + \mathbf{f} - \rho \ddot{\mathbf{u}} \right] dV = 0 \tag{1.15}$$

Since the equation 1.15 is valid for arbitrary volume V, the integrand vanishes everywhere and we obtain the momentum equation [2]

$$\nabla \cdot \tau + \mathbf{f} - \rho \ddot{\mathbf{u}} = 0 \tag{1.16}$$

in absence of body forces, we have the homogeneous equation of motion

$$\nabla \cdot \tau - \rho \ddot{\mathbf{u}} = 0 \tag{1.17}$$

that governs seismic wave propagation outside source regions.

1.2.2 Seismic wave equation

In order to solve the equation 1.17 we require a relationship between stress and strain so that we can express τ in terms of displacement $\mathbf{u}$. Recall the linear, isotropic stress-strain relationship 1.9 and the definition of strain tensor 1.4 we obtain:

$$\tau_{ij} = \lambda \delta_{ij} \partial_k u_k + \mu(\partial_i u_j + \partial_j u_i) \tag{1.18}$$

If we substitute equation 1.18 in equation 1.17 we can write in vector notation

$$\rho \ddot{\mathbf{u}} = \nabla \lambda (\nabla \cdot \mathbf{u}) + \nabla \mu \cdot [\nabla \mathbf{u} + (\nabla \mathbf{u})^T] + (\lambda + \mu)\nabla \nabla \cdot \mathbf{u} + \mu \nabla^2 \mathbf{u} \tag{1.19}$$

We use the vector identity

$$\nabla^2 \mathbf{u} = \nabla \nabla \cdot \mathbf{u} - \nabla \times \nabla \times \mathbf{u} \tag{1.20}$$

to obtain the seismic wave equation [3]:

$$\rho \ddot{\mathbf{u}} = \nabla \lambda (\nabla \cdot \mathbf{u}) + \nabla \mu \cdot [\nabla \mathbf{u} + (\nabla \mathbf{u})^T] + (\lambda + 2\mu)\nabla \nabla \cdot \mathbf{u} - \mu \nabla \times \nabla \times \mathbf{u} \tag{1.21}$$

The first two terms on the right-hand side involve gradients in the Lamé parameters themselves and are non zero whenever the material is inhomogeneous. Furthermore, we can consider the velocity as a function only of dept, then the material can be modeled as a series of homogeneous layers. Within each layer, there are no gradient in the Lamé parameters and so these terms go to zero. The different solutions of each layer are linked by calculating the reflection and transmission coefficients for waves at both side of the interface separating the layers. The effects of a continuous velocity gradient can be simulated increasing the number of layers. Then, if we ignore the gradient terms, the momentum equation for homogeneous media becomes:

$$\rho \ddot{\mathbf{u}} = (\lambda + 2\mu)\nabla \nabla \cdot \mathbf{u} - \mu \nabla \times \nabla \times \mathbf{u} \tag{1.22}$$

that is the standard form for seismic wave equation [1] [2] [3]. However, it is important to remember that it is an approximate equation, which neglects the gravity and the velocity gradient terms and assumes a linear, isotropic Earth model.

1.2.3 P- and S- waves

We can separate the equation 1.22 into solution for P-waves and S-waves by taking the divergence and the curl, respectively. Taking the divergence of equation 1.22 and using the vector identity $\nabla \cdot \nabla \times \boldsymbol{\Psi} = 0$, we obtain

$$\nabla^2(\nabla \cdot \mathbf{u}) - \frac{1}{\alpha^2}\frac{\partial^2(\nabla \cdot \mathbf{u})}{\partial t^2} = 0 \qquad (1.23)$$

where the P-wave velocity, α, is given by

$$\alpha^2 = \frac{\lambda + 2\mu}{\rho} \qquad (1.24)$$

Taking the curl of equation 1.22 and using the vector identity $\nabla \times \nabla\phi = 0$, we obtain

$$\nabla^2(\nabla \times \mathbf{u}) - \frac{1}{\beta^2}\frac{\partial^2(\nabla \times \mathbf{u})}{\partial t^2} = 0 \qquad (1.25)$$

where the S-wave velocity, β, is given by

$$\beta^2 = \frac{\mu}{\rho} \qquad (1.26)$$

A table of typical seismic waves velocities is shown in table 1.3.

Potentials

The displacement $\mathbf{u}$ is often expressed in terms of the P-wave scalar potential ϕ and S-wave vector potential $\boldsymbol{\Psi}$, using the Helmholtz decomposition theorem[2]:

$$\mathbf{u} = \nabla\phi + \nabla \times \boldsymbol{\Psi} \qquad \text{with } \nabla \cdot \boldsymbol{\Psi} \qquad (1.27)$$

We then have

$$\nabla \cdot \mathbf{u} \;=\; \nabla^2\phi \qquad (1.28)$$

$$\nabla \times \mathbf{u} \;=\; -\nabla^2\boldsymbol{\Psi} \qquad \text{since } \nabla \cdot \boldsymbol{\Psi} = 0 \qquad (1.29)$$

---

[2]Each differentiable field can be expressed as the gradient of scalar field plus the curl of vectorial field.

Rock/Soil Description	Average S-wave velocity (m/s)
Hard Rock	>1500
Rock	760-1500
Very dense soil/soft rock	360-760
Stiff soil	180-360
Soft soil	<180
Rock/Soil Description	**Average P-wave velocity (m/s)**
Air	330
Water	1450-1530
Sand (dry, loose)	200-1000
Sand (water saturated, loose)	1500-2000
Sand and gravel	400-2300
Clay	1000-2500
Sandstone	2500-4500
Limestone (soft)	1700-4200
Limestone (hard)	2800-7000
Dolomites	2500-6500
Shales	2000-4100
Granites	4600-6200
Basalts	5500-6500
Serpentinite	5500-6500
Gneiss	3500-6500
Concrete	3000-3500

Figure 1.3: P- and S- wave velocities for different materials.

Substituting into 1.23 and 1.25, we may obtain

$$
\begin{aligned}
\nabla^2 \phi - \frac{1}{\alpha^2}\frac{\partial^2 \phi}{\partial t^2} &= 0 \\
\nabla^2 \boldsymbol{\Psi} - \frac{1}{\beta^2}\frac{\partial^2 \boldsymbol{\Psi}}{\partial t^2} &= 0
\end{aligned}
\tag{1.30}
$$

The P-wave solution is given by the scalar wave equation for ϕ; the S-wave solution is the vector wave equation for $\boldsymbol{\Psi}$.

Polarization of P- and S- waves

The general solutions of equations 1.30 are plane waves described by general function:

$$
\mathbf{u}(\mathbf{x}, t) = \mathbf{A}(\omega)e^{i(\mathbf{k}\cdot\mathbf{x} - \omega t)}
\tag{1.31}
$$

where $\mathbf{k} = (\omega/c)\hat{\mathbf{k}}$ is the wave vector and c the phase velocity of the wave. Other parameters and their relationship are shown in table 1.1.

Consider the equation for P-wave. Because $\mathbf{u} = \nabla\phi$, we have $u_x = \partial_x\phi$, $u_y = 0$ and $u_z = 0$. Note that for a plane wave propagating in the x direction there is no

13

Name	Symbol	Relationship
Angular frequency	ω	$\omega = 2\pi f = 2\pi/T = ck$
Frequency	f	$f = \omega/(2\pi) = 1/T = c/\Lambda$
Period	T	$T = 1/f = (2\pi)/\omega = \Lambda/c$
Velocity	c	$c = \Lambda/T = f\Lambda = \omega/k$
Wavelength	Λ	$\Lambda = c/f = cT = 2\pi/k$
Wave vector	k	$k = \omega/c = 2\pi/\Lambda = 2\pi f/c$

Table 1.1: Harmonic wave parameters

change in the y and z direction, so the spatial derivative ∂_y and ∂_z are zero. For P-waves, the only displacement occurs in the direction of propagation along the x axis. Such wave is termed longitudinal. Also, because $\nabla \times \nabla \phi = 0$ the motion is curl-free or irrotational. Since P-waves introduce volume changes in the material ($\nabla \cdot \mathbf{u} \neq 0$), they can also be termed compressional or dilatational. However, note that P-waves involve shearing as well as compression; this is why the P velocity is sensitive to both the bulk and shear moduli.

Now consider a plane S-wave propagating in the positive x direction. The displacement is

$$
\begin{aligned}
u_x = (\nabla \times \boldsymbol{\Psi})_x &= \partial_z \Psi_y - \partial_y \Psi_z = 0 \\
u_y = (\nabla \times \boldsymbol{\Psi})_y &= \partial_x \Psi_z - \partial_x \Psi_z = \partial_x \Psi_z \\
u_z = (\nabla \times \boldsymbol{\Psi})_z &= \partial_y \Psi_x - \partial_x \Psi_y = -\partial_x \Psi_y
\end{aligned}
\tag{1.32}
$$

thus giving

$$
\mathbf{u} = \partial_x \Psi_z \hat{\mathbf{y}} - \partial_x \Psi_y \hat{\mathbf{z}}
\tag{1.33}
$$

The motion is in the y and z direction, perpendicular to the propagation direction. S-wave particle motion is often divided in two components: the motion within a vertical plane through the propagation vector (SV-waves) and the horizontal motion

14

in the direction perpendicular to this plane (SH-wave). Because $\nabla \cdot \mathbf{u} = \nabla \cdot (\nabla \times \mathbf{\Psi}) = 0$, the motion is pure shear without any volume change.

Particle motion for harmonic P-wave and for harmonic shear wave polarized in the vertical direction (SV-wave) is illustrated in figure 1.4.
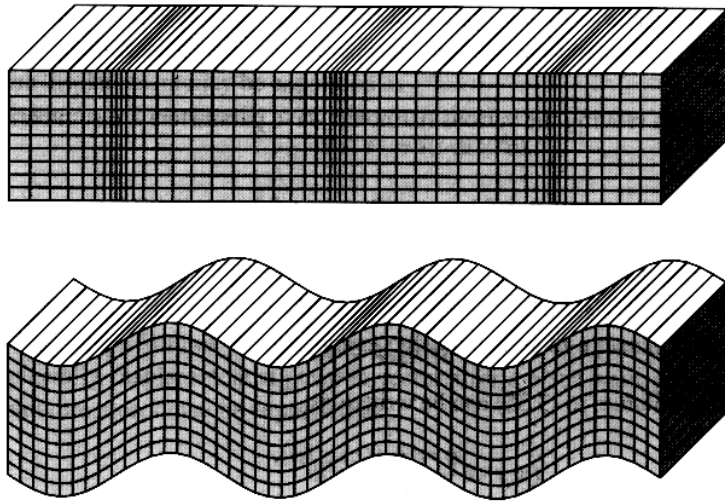
Figure 1.4: Displacement occurring from a harmonic plane P-wave (top) and S-wave (bottom) traveling horizontally.

1.3   Surface waves

Our treatment to this point has been limited to body waves, solutions to the seismic wave equation which exist in whole spaces. However, when free surfaces exist in a medium, other solutions are possible and are called surface waves. There are two types of surface waves that propagate along Earth's surface, Rayleigh waves and Love waves. For laterally homogeneous models, Rayleigh waves are radially polarized (P/SV) and exist at any free surface, whereas Love waves are transversely polarized and require some velocity increase with depth (or a spherical geometry). Surface waves are generally the strongest arrivals recorded at teleseismic distances

and they provide some of the best constraints on Earth's shallow structure and low-frequency source properties. They differ from body waves in many respects: they travel more slowly, their amplitude decay with range is generally smaller, and their velocities are strongly frequency dependent.

1.3.1   Love waves

Love waves are formed through the constructive interference of high order SH surface multiples, i.e. SSS, SSSS, SSSSS, etc. (for more details see [2] [3]). Thus, It is possible to model Love waves as a sum of body waves. To see this, consider monochromatic plane wave propagation for the case of a vertical velocity gradient in a laterally homogeneous model. In this case, a plane wave defined by ray parameter p will turn at the depth where $\beta = 1/p$.

Along the surface the plane waves will propagate with horizontal slowness defined by p. If the surface bounce points are separated by a distance $X(t)$, then the travel time along the surface between bounce points is given by $pX(p)$. This follows from our definition of a plane wave and does not depend upon the velocity model. In contrast, the travel time along the ray paths is given by $T(p)$ and is a function of the velocity-depth profile (see figure 1.5). If these travel times are not the same, as it generally happens, destructive interference will occur except at certain fixed frequencies. Along the surface, the phase (0 to 2π) of an harmonic wave will be delayed by $\omega pX(p)$, where ω is the angular frequency of the plane wave.

The phase along the ray path is delayed by $\omega T(p) - \pi/2$, so the requirement for constructive interference is

$$\omega = \frac{n2\pi + \pi/2}{T(p) - pX(p)} \qquad \text{with is an integer} \qquad (1.34)$$

The wave travels along the surface at velocity $c = 1/p$, thus the equation 1.34 defines the $c(\omega)$ function for the Love waves, often termed as dispersion curve. The values
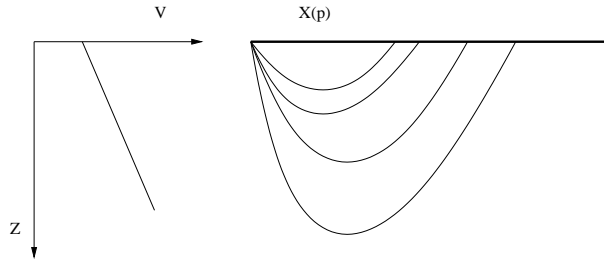
16

Figure 1.5: Ray paths $T(p)$ (on the right) for a model with a continuous velocity increase with depth (on the left) will curve back toward the surface.

of ω given $n = 0$ are termed the fundamental modes; highest modes are defined by larger values of n. The frequency dispersion in the Love waves results from ray geometry and does not require any frequency dependence in the body wave velocity β.

The velocity defined by c is the velocity with which the peaks and troughs at a given frequency move along the surface and is termed phase velocity. When the phase velocity varies as a function of frequency, as in equation 1.34, the wave is dispersed and the group velocity (the velocity with which the energy propagates) will be different from the phase velocity. In the Love waves, the energy must move along the actual ray path and thus the group velocity U is defined by

$$U = \frac{X(p)}{T(p)} \tag{1.35}$$

The relationship between the phase velocity and the group velocity is shown in figure 1.6 as a sum of SH surface waves.

1.3.2 Rayleigh Waves

For SH polarized waves, the reflection coefficient at the free surface is one, and the interference between the downgoing SH-waves and those turned back toward the surface produces Love waves. The P/SV system is more complicated because
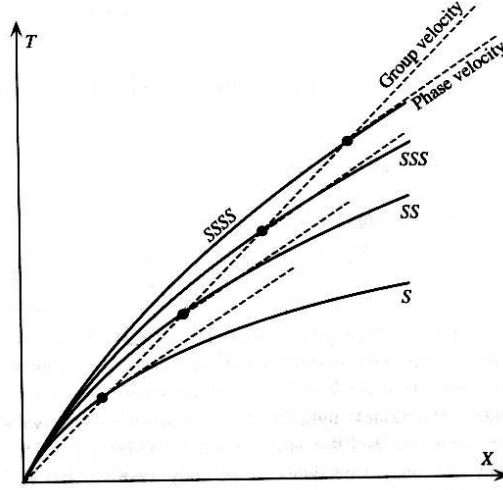
17

Figure 1.6: The relationship between the phase velocity and the group velocity is shown. The dashed lines show the group and the phase velocities at a fixed value of the ray parameter p.

the surface reflections involve both P- and SV-waves. In this case, the upgoing ad downgoing body waves do not sum constructively to produce surface waves. However, a solution is possible for inhomogeneous waves trapped at the interface: the resulting surface waves are termed Rayleigh waves [2] [3].

Let us begin by examining what occurs when P- and SV-waves interact with a free surface. For a laterally homogeneous medium, the displacements for harmonic plane waves propagating in the $+x$ direction are given by

$$\mathbf{u} = \mathbf{A}e^{-i\omega(t-px-\eta x)} \tag{1.36}$$

where p is the horizontal slowness and $\eta = \sqrt{1/c^2 - p^2}$ is the vertical slowness for the wave velocity c. Now for equation 1.36, consider a plane wave solution for ϕ and Ψ_y (the only part of $\mathbf{\Psi}$ that produces SV motion for plane wave propagation in the x direction):

$$\phi = Ae^{-i\omega(t-px-\eta_\alpha z)} \tag{1.37}$$

18

$$\Psi_y \quad = \quad Be^{-i\omega(t-px-\eta_\beta z)} \tag{1.38}$$

where A and B are the amplitude of P- and SV-waves respectively, and the vertical slownesses are η_α and η_β. The ray parameter p is constant and both P- and SV are assumed to have the same horizontal slowness.

Now consider the boundary conditions at the free surface ($z = 0$). Both the normal and the shear traction must vanish, and, recalling the equation 1.9 it is possible to obtain a set of equations for the ray parameter and for the vertical slownesses:

$$\begin{aligned} A(2p\eta_\alpha) - B(p^2 - \eta_\beta^2) &= 0 \\ A[\alpha^2(p^2 + \eta_\alpha^2) - 2\beta^2 p^2] - B(2\beta^2 \eta_\beta p) &= 0 \end{aligned} \tag{1.39}$$

This coupled set of equations describes the free surface boundary condition for P- and SV-waves with horizontal slowness p. When $p < 1/\alpha$, there are two real solutions, a positive value of η_α for down-going P-waves and a negative value for up-going P-waves (assuming the z axis points down-going). Similarly, when $p < 1/\beta$, then η_β is real and there exist both down-going and up-going SV-waves.

However, our interest is in the case of $p > \beta^{-1} > \alpha^{-1}$ and both η_α and η_β are imaginary. In this case the equation 1.36 becomes

$$\mathbf{u} = \mathbf{A}e^{i\omega\eta z}e^{-i\omega(t-px)} \tag{1.40}$$

and we see that imaginary values of η will lead to real values in the exponents and so the wave amplitude decays exponentially as a function of depth. For $z = 0$ we have only single imaginary values of η and the linear system of equation for A and B given in 1.39 has a non trivial solution only when the determinant vanishes. Substituting for η_α and η_β, we can obtain an equation involving the ray parameter p and the body waves velocities α and β.

$$\left(2p^2 - \frac{1}{\beta^2}\right)^2 - 2p^2\left(p^2 - \frac{1}{\alpha^2}\right)^{1/2}\left(p^2 - \frac{1}{\beta^2}\right)^{1/2} = 0 \tag{1.41}$$

This is termed the Rayleigh function and has a single solution, with the exact value of p depending upon α and β. Using the solution for p we can obtain the relative amplitude of the P and SV components and so, using the relations 1.27, also the vertical and horizontal displacements. Particle motion for both Love and Rayleigh waves are compared in figure 1.7.
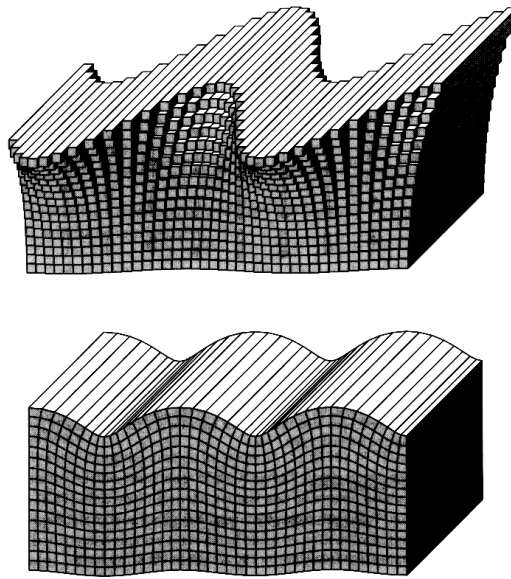

Figure 1.7: Displacement occurring from a Love (top) and Rayleigh (bottom) traveling horizontally. Love waves are purely transverse motion, whereas Rayleigh waves contain both vertical and radial motion. In both case, the wave amplitude decays strongly with depth.

1.4 Seismometers

In this first chapter we have discussed Earth motion in terms of the displacement field $\mathbf{u}(\mathbf{x}, t)$, but we have not mentioned how these movements are actually recorded. A device that detects seismic wave motion is termed seismometer; the entire instrument package, including the recording apparatus, is called seismograph. The most

common type of seismometer is based on the inertia of a suspended mass, which tend to remain stationary in response to external vibrations. As an example, figure 1.8 shows a simple seismometer scheme that will detect vertical ground motion.
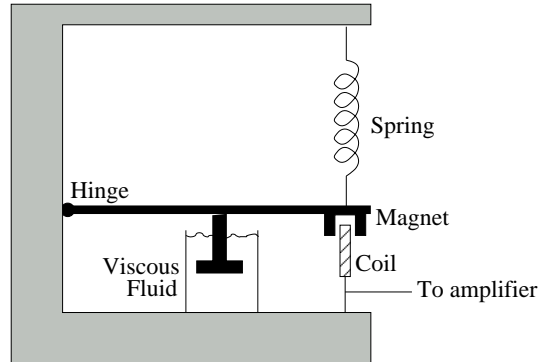

Figure 1.8: A simple inertial seismometer for measuring vertical motion.

A mass is suspended from a spring and connected to a lever such that it can move only in the vertical direction. Motions in the lever are dumped using a "dash pot" to prevent excessive oscillations near the resonant frequency of the system. The differential motion between the mass and the seismometer case (which is rigidly connected to Earth) is measured using the voltage induced in a coil by the motion of a magnet. The induced voltage is proportional to the velocity of the mass for the instrument shown in figure 1.8. In alternative seismometer designs, the displacement or acceleration of the mass may be measured. Another scheme, which is similar to the one shown in figure 1.8, can be used to detect horizontal ground motion; in this case the mass is suspended as a pendulum. Both vertical and horizontal suspended mass instrument are called inertial seismometers.

1.4.1 Force feedback seismometer

The best modern instruments are more sophisticated than the simple mechanical seismograph illustrated in figure 1.8. They are designed to achieve a linear response

to Earth motion over a wide range of both amplitude and frequency. Mechanical non-linearity can arise from the finite length of the springs and levers used in the design. For example, the design shown in figure 1.8 will be linear only for excursions of the mass which are small compared to the length of the lever arm. Linearity is often maintained in modern instrument through the use of force-feedback designs in which the mass is maintained at fixed point. The seismograph records a measure of the force that is required to keep the mass at rest; this force is directly related to Earth acceleration. For example we discuss the functionality of a standard seismometer, the "EpiSensor model FBA ES-T" of Kinemetric©.

The Episensor consists of three orthogonally mounted force balance accelerometers (FBAs), X-axis, Y-axis and Z-axis, inside a sensor casing. Each accelerometer module is identical and plugs into a board that provides the final output circuit and the carrier oscillator. The figure 1.9 shows a simplified block diagram of the major components of each of the FBAs.
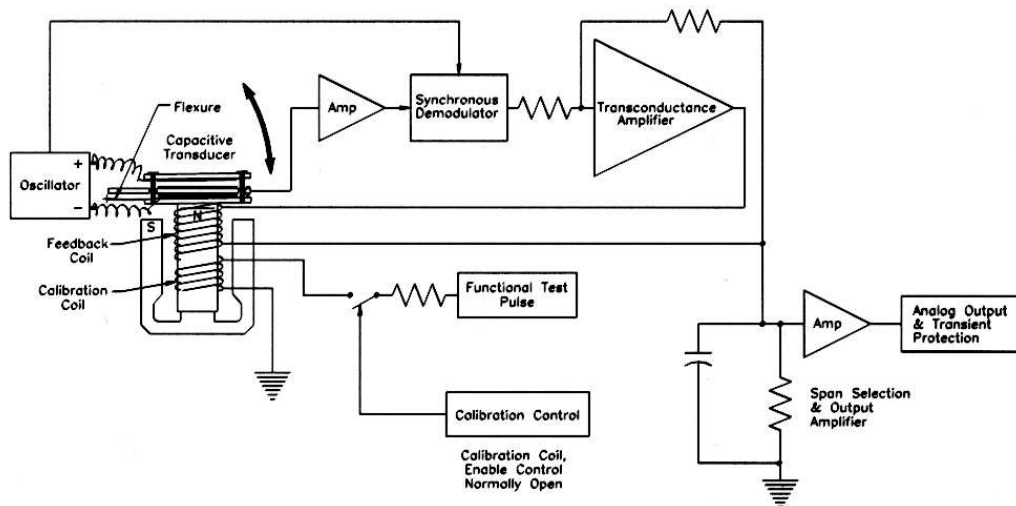

Figure 1.9: Simplified block diagram of an accelerometer.

The working principles are the following:

- the oscillator applies an AC signal of opposite polarity to two moving capacitor plates (also referred to as the moving mass). When the accelerometer is zeroed and when no acceleration is applied, these applied are symmetrical to the fixed central plate and no voltage is generated.

- An acceleration causes the coil and capacitive sensor plate, which are a single assembly mounted on mechanical flexures (springs), to move with respect to the fixed central plate of the capacitive transducer.

- This displacement results in a signal on the center plate of the capacitor becoming unbalanced, resulting in an AC signal of the same frequency as the oscillator being passed to the amplifier.

- The amplifier amplifies this AC signal. This error signal is then passed to the demodulator where it is synchronously demodulated and filtered, creating a DC error term in the feedback amplifier.

- The feedback loop compensates for this error signal by passing current through the coil to create a magnetic restoring force to balance the capacitor plates back to their original null position.

- The current traveling through the coil is thus directly proportional to the applied acceleration. By passing this current through a complex impedance consisting of a resistor and capacitor, it can be converted to a voltage output proportional to acceleration with a bandwidth of approximately $200\,Hz$.

- Selecting a particular resistor value sets the full-scale range. The resistor values are determined by a high accuracy network, so the range can be set at $g/4$, $g/2$, g, $2g$ and $4g$, where g is the gravity acceleration.

- The capacitor and overall loop again are selected along with the resistor to ensure an identical transfer function on each range.

- The voltage output of the resistor capacitor network is set to $2.5\,V$ for the acceleration value corresponding to the particular range. This voltage is then passed into a low-power and low-noise amplifier that amplifies this signal by either 1 or 4 to give a single-ended output of either $\pm 4\,V$ or $\pm 10\,V$.

- A second amplifier is also present which inverts the signal from the first and can be connected to the negative output lead. This allows the unit to give a differential $\pm 5\,V$ or $\pm 20\,V$ to match the input to digitizers.

It is possible to determine a good empirical model of the system, which uses two pair of conjugate poles to represent the transfer function of the instrument. If this transfer function is corrected for the DC sensitivity of the sensor, the amplitude agreement is within $\pm 0.5\,dB$ over the bandwidth of the sensor. This model can be represented as

$$\frac{V(s)}{A(s)} = \frac{k_1 k_2}{(s - p_1)(s - p_2)(s - p_3)(s - p_4)} \tag{1.42}$$

where $k_1 = 2.46 \cdot 10^{13}$, k_2 is the sensitivity in V/g, $p_{1,2} = -981 \pm 1009i$, $p_{3,4} = -3290 \pm 1263i$, $V(s)$ is the Laplace transform of the output voltage and $A(s)$ is the Laplace transform of the input acceleration. The amplitude of the transfer function 1.42 is shown in figure 1.10. Remember that the episensor has a dynamic range of $155dB$ in the frequency band $0 \div 200\,Hz$ and its sensitivity is $80V/g$, in differential mode with a full scale range of $\pm g/4$,

1.4.2 Classification of modern seismometer

Modern seismometers can be roughly divided into three types by purpose of use: sensitivity seismometers for earthquake research observation, strong-motion seismometers for earthquake engineering , and control-type seismometers for secondary disaster prevention.
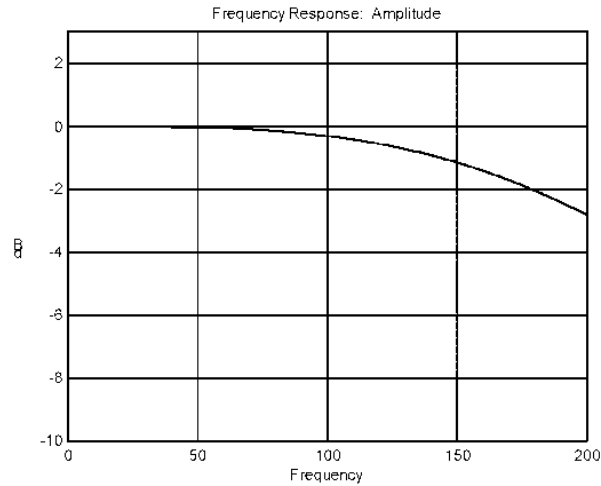
Figure 1.10: Amplitude transfer function of the episensor.

- Sensitivity seismometers for earthquake research observation: a typical sensitivity seismometer is an electrodynamic seismometer. This kind of seismometer measures micro earthquakes, that the human body cannot feel. This seismometer is required to detect the rising part of the waveform of P- and S-waves, which will be necessary for determining the hypocenter, and to record the exact times. To ensure this sensitivity observation, it is essential to eliminate miscellaneous man-made vibrations. Thus, sensitivity seismometers should be installed in earthquake observation stations distant from urban cities or in very deep underground observation bore.

- Strong-motion seismometers for earthquake engineering: a strong-motion seismometer mainly refers to a seismometer used to record how the ground under a structure responds to strong earthquake motions. Strong-motion seismometers start up only after they detect an earthquake greater than a preset level. They use their vertical movement components to detect the earliest P-waves, and this detection starts them up. They record waveform data with a delay circuit of ten seconds. It does take some time to cause the circuit to rise, but

25

the seismometers can actually obtain the waveform that was generated earlier than the seismometers started recording. The earthquake data, including waveform, will be recorded in an IC card. The data stored can be remotely accessed through the public telephone line. Thus, data from multiple locations can be collected and managed. Modern seismometers are computer systems with communication capability and with internal sensitivity sensors, rather than mere mechanical seismometers. The conventional seismometers were used solely for recording waveforms. The combined use of high-performance sensors, such as servo acceleration sensors, and a micro processor has changed this conventional seismometer into a new recording system equipped with multiple channels and functions. The new strong-motion sensor also collects wind direction and speed data along with seismic data. For this reason, the modern seismometer is also used as a disaster prevention system.

- Control-type seismometers for secondary disaster prevention: control-type seismometers issue an alarm signal immediately after an earthquake motion greater than a preset level occurs. These seismometers are not necessarily required to record seismic waves. However, they do need to offer accuracy and reliability that are different from those seen in other seismometers, since malfunction will directly cause huge economical loss or social disorder. These control-type seismometers are used to protect the infrastructure of our modern society, including railroads, nuclear plants, petrochemical complexes, and power and gas facilities. One of the familiar examples of use of the control-type seismometer is the emergency shut-down system to stop elevators in case of an earthquake. The simplified type is often interlocked with an automatic broadcast system in places where people gather, such as department stores and banks, in order to prevent panics in case of an earthquake. Display-type seismometers are used to display the extent of damage and the correct seismic

intensity immediately after an earthquake. This information will be useful for evacuation and safety activities.

1.4.3 Laser Techniques

In the last years, several instruments, based on light interference phenomena, have been developed. In the section 2.1 the interference phenomena will be discussed, while in this paragraph we just show a lot of this kind of instruments.

The first class of interferometric sensors for seismic applications are strainmeters: they are built to measure the time variation of either linear strain, areal strain, shear strain, or volumetric strain. Largely used for geophysical purposes are extensometers, which measure the variation of distance between two fixed points in cavities, mines, or trenches (or, occasionally, on the surface). The class of laser strainmeters date back to the 1960s, and consist of a long path Fabry Perot or a Michelson interferometer. The variations of length are detected with a sensitivity of 10^{-9} on baselines $\approx 10^2\,m$. For more details we refer to [6], [7], [8], [9], [10] and [11].

The second class of interferometric sensor are accelerometer in which the reading system of the oscillating component is based on light interferometry. For examples we refer the work [12], [14] and [13]. Anyway we have not found any commercial sensors, based on interferometry, for geophisics applications.

Chapter 2

Interferometric seismic sensors

2.1 Optical Interferometry

The theory of optical interference is based essentially on the principle of the linear superposition of electric field. According to this principle, the electric field $\mathbf{E}$ produced at a point in the empty space jointly by several different sources is equal to the vector sum of the field produced by the different sources. The same is true for the magnetic field. This principle is a consequence of the fact that the Maxwell's equations are linear differential equations.

Let us consider two plane harmonic waves of the same angular frequency ω. The electric fields are then

$$
\begin{aligned}
\mathbf{E}_{(1)} &= \mathbf{E}_1 \exp(i(\mathbf{k_1} \cdot \mathbf{r} - \omega t + \phi_1)) \\
\mathbf{E}_{(2)} &= \mathbf{E}_2 \exp(i(\mathbf{k_2} \cdot \mathbf{r} - \omega t + \phi_2))
\end{aligned}
\tag{2.1}
$$

Here the quantities ϕ_1 and ϕ_2 have been introduced to allow for any phase difference between the sources of the two waves. If the difference $\phi_1 - \phi_2$ is constant, the two sources are said to be *mutually coherents* and also the resulting waves are termed mutually coherents. The irradiance at a point is proportional to the square of the

amplitude of the light field at the point in question. Thus the superposition of two monochromatic plane waves, aside from a constant proportionality factor, result in an irradiance function

$$
\begin{aligned}
I = |\mathbf{E}|^2 = \mathbf{E} \cdot \mathbf{E}^* &= (\mathbf{E}_{(1)} + \mathbf{E}_{(2)}) \cdot (\mathbf{E}^*_{(1)} + \mathbf{E}^*_{(2)}) = \\
&= |\mathbf{E}_1|^2 + |\mathbf{E}_2|^2 + 2E_1 E_2 \cos\theta = \\
&= I_1 + I_2 + 2E_1 E_2 \cos\theta
\end{aligned}
\tag{2.2}
$$

where

$$
\theta = \mathbf{k}_1 \cdot \mathbf{r} - \mathbf{k}_2 \cdot \mathbf{r} + \phi_1 - \phi_2
\tag{2.3}
$$

The term $2E_1 E_2 \cos\theta$ is called the *interference term* and it indicates that I can be greater or smaller than the sum $I_1 + I_2$, depending on the value of θ. These variations are the interference fringes that are seen when two mutually coherent beams of light are combined. If the sources of two waves are not mutually coherent, then the quantity θ, defined in the equation 2.3, varies with time in a random fashion. The result is that the mean value of $\cos\theta$ is zero, and there is no interference. This is the reason for which interference fringes are not observed with two separate light sources.

In the case of partial coherence of two sources 1 and 2, the irradiance I can be expressed as

$$
I = <\mathbf{E} \cdot \mathbf{E}^*> = <|\mathbf{E}_1|^2 + |\mathbf{E}_2|^2 + 2\mathrm{Re}(\mathbf{E}_{(1)} \cdot \mathbf{E}^*_{(2)})>
\tag{2.4}
$$

where the sharp brackets denote the time average. If we assume that all quantities are stationary and that the optical fields have the same polarization, the equation 2.4 can be written as

$$
I = I_1 + I_2 + 2\mathrm{Re} < (\mathbf{E}_1 \cdot \mathbf{E}^*_2 >
\tag{2.5}
$$

Let us define the *mutual coherence function* of the two field E_1 and E_2:

$$
\Gamma_{12}(\tau) = < (E_1(t) \cdot E^*_2(t + \tau) >
\tag{2.6}
$$

and the *self-coherence function*

$$\Gamma_{11}(\tau) = < (E_1(t) \cdot E_1^*(t + \tau) > \tag{2.7}$$

from the definition we see that $\Gamma_{11}(0) = I_1$ and $\Gamma_{22}(0) = I_2$. If we use a normalized correlation function called *degree of partial coherence*:

$$\gamma_{12} = \frac{\Gamma_{12}(\tau)}{\sqrt{I_1 I_2}} \tag{2.8}$$

then the irradiance can be expressed as follows:

$$I = I_1 + I_2 + 2\sqrt{I_1 I_2} \text{Re}(\gamma_{12}(\tau)) \tag{2.9}$$

Thus, in term of $|\gamma_{12}|$ we have the following type of coherence

$$|\gamma_{12}| = 1 \qquad \text{Complete coherence}$$

$$0 < |\gamma_{12}| < 1 \qquad \text{Partial coherence}$$

$$|\gamma_{12}| = 0 \qquad \text{Complete incoherence}$$

In the patter of interference fringes, the intensity varies between two limits, I_{max} and I_{min}. If we define the *fringe visibility* as

$$V = \frac{I_{max} - I_{min}}{I_{max} + I_{min}} \tag{2.10}$$

it follows that

$$V = \frac{2|\gamma_{12}|\sqrt{I_1 I_2}}{I_1 + I_2} \tag{2.11}$$

In particular, if $I_1 = I_2$, then $V = |\gamma_{12}|$, that is, the fringe visibility is equal to the modulus of the degree of partial coherence. In the case of complete coherence the interference fringes have the maximum contrast of unity, whereas for complete incoherence the contrast is zero; that is, there are no interference fringes at all.
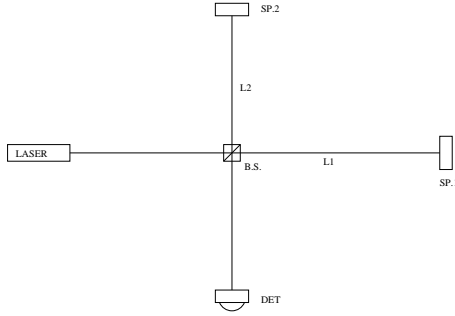
Figure 2.1: Optical scheme of a Michelson inteferometer

2.2   Model of interferometric seismic sensor

The best and most versatile interferometric device is the interferometer developed by Michelson in 1880. The basic designed is shown in figure 2.1. The electromagnetic field E_{in} from the source falls on a lightly silvered glass plate (Beam Splitter, Bs), that divides the beam in two parts. These separated beams are reflected back to Bs by the mirror S_1 and S_2, as shown. The interference patters is observed in E_{out}.

Assuming a plane wave beam, the Michelson interferometer output, $I(t)$, can be generally expressed as

$$I(t) = I_{min} + \frac{I_{max} - I_{min}}{2} \left[1 + \cos(\phi(t))\right] \qquad (2.12)$$

where $\phi(t)$ is the phase difference between the two beam, and I_{max} and I_{min} are the maximum and the minimum output intensities, respectively. In particular, the maximum value of the intensity is reached when the two beams are recombined in phase, while the minimum is instead obtained when they are recombined in opposition of phase. Generally, these quantities are time dependent, but for a Michelson Interferometer with well aligned mirrors and nearly equal arm lengths, negligible laser source amplitude noise and coherent length of the laser source much longer than the arm lengths, we can consider them constant. Therefore, the only time

dependent quantity in equation 2.12 is the phase change $\phi(t)$, expressed as

$$\phi(t) = \frac{4\pi n(t)}{\lambda(t)} \left\{ [l_2(t) - l_1(t)] + \sum_{i=1}^{2} [l_i(t) + d] \sum_{j=1}^{2} \theta_{i,j}^2 \right\} \tag{2.13}$$

where $\lambda(t)$ is the laser beam wavelength, $n(t)$ is the spatial mean refraction index, $l_i(t)$ is the ith arm-length, d is the distance of the beam-splitter from the output photodiode, and $\theta_{i,j}$ is the jth tilt of the mirror in the ith arm.

Note that all these functions are in principle time dependent. To understand the time evolution of the phase it is necessary to calculate the total derivative

$$\dot{\phi}(t) = \frac{d\phi}{dt} = \frac{\phi(t)}{n(t)}\dot{n} - \frac{\phi(t)}{\lambda(t)}\dot{\lambda} - \frac{4\pi n(t)}{\lambda(t)}\frac{d(l_2 - l_1)}{dt} +$$
$$+ \frac{4\pi n(t)}{\lambda(t)} \left[(\theta_{1,1} + \theta_{1,2})\dot{l}_1 + (\theta_{2,1} + \theta_{2,2})\dot{l}_2 \right] +$$
$$+ \frac{4\pi n(t)}{\lambda(t)} \left[(l_1 + d)(\dot{\theta}_{1,1} + \dot{\theta}_{1,2}) + (l_2 + d)(\dot{\theta}_{2,1} + \dot{\theta}_{2,2}) \right] \tag{2.14}$$

Considering finite quantity, the total phase variation due to each time dependent quantity is the following:

$$\Delta\phi(t) = \frac{\phi(t)}{n(t)}\Delta n$$

$$\Delta\phi(t) = \frac{\phi(t)}{\lambda(t)}\Delta\lambda$$

$$\Delta\phi(t) = \frac{4\pi n(t)}{\lambda(t)}(\theta_{1,1} + \theta_{1,2})\Delta l_1$$

$$\Delta\phi(t) = \frac{4\pi n(t)}{\lambda(t)}(\theta_{2,1} + \theta_{2,2})\Delta l_2$$

$$\Delta\phi(t) = \frac{4\pi n(t)}{\lambda(t)}\Delta(l_2 - l_1)$$

$$\Delta\phi(t) = \frac{4\pi n(t)}{\lambda(t)}(l_1 + d)\Delta\theta_{1,1}$$

$$\Delta\phi(t) = \frac{4\pi n(t)}{\lambda(t)}(l_1 + d)\Delta\theta_{1,2}$$

$$\Delta\phi(t) = \frac{4\pi n(t)}{\lambda(t)}(l_2 + d)\Delta\theta_{2,1}$$

$$\Delta\phi(t) = \frac{4\pi n(t)}{\lambda(t)}(l_2 + d)\Delta\theta_{2,2} \tag{2.15}$$

Using these equation it is possible to calculate the phase error due to the geometrical fluctuation of the interferometer components. It is important to note that these errors depend critically by experimental setup.

Furthermore, since techniques exist allowing to perform the alignment control of the optics in a way completely independent from the longitudinal degrees of freedom, it is possible to introduce the hypothesis of a perfectly aligned system, so that the equation 2.13 can be written as

$$\phi(t) = \frac{4\pi n(t)}{\lambda(t)} l_{eq}(t) \tag{2.16}$$

where $l_{eq}(t) = l_2(t) - l_1(t)$ is the longitudinal Michelson interferometer arm-length difference, that is of course a time dependent function. Then, to extract the arm-length change due to the presence of a seismic wave, we choose one arm as reference, mechanically fixing its length and protecting it from refraction index changes, which may simulate mechanical length changes. The other arm, that is the measurement arm, is instead allowed to change its length in order to measure the passage and the amplitude of a seismic wave.

Note that in this model we did not take into any account the transfer function of the mechanical mounting on which the mirrors of the interferometer are mounted. If the effect of the mounting must be taken into account because it has effects in the interferometer measurement band then, assuming that the mechanical mountings have only linear effects on the output, it is possible to express the output of the interferometer as the convolution of the input signal and the mechanical mountings impulse response, that is

$$\Delta l_{eq}(t) = k_2(t) * l_2(t) - k_1(t) * l_1(t) \tag{2.17}$$

where $k_1(t)$ and $k_2(t)$ are the impulse response of the mechanical mounting relative to the mirror 1 and to the mirror 2, respectively. In particular, if the mechanical mountings are the same for both the mirrors then $k_1(t) = k_2(t) = k(t)$ and

$l_{eq}(t) = k(t) * (l_2(t) - l_1(t))$. Furthermore note that the oscillations of the optical holders induced by ground motion are anyway at frequencies enough high to be attenuated by the low pass anti-aliasing filters located before the ADCs and so we can approximate $k(t) = 1$.

Two further approximation can be done. The first approximation consist in assuming the laser wavelength enough stable so that the time dependent of the λ function can be considered constant for our purpose. This approximation can be done using a stabilized laser source. These laser system provide high levels of frequency and intensity reference for precision applications that are dependent or enhanced by a single, invariant frequency, such interferometry. The ultra stable, narrow band, single longitudinal output enables highly repeatable and highly accurate measurements with enhanced resolution. For example, we can consider the stabilized laser system model 05-STP-903 of Melles-Griot. It has frequency (nominal) $f = 473.61254\,THz$, frequency stability guaranteed $\Delta f = \pm 2.0\,MHz$ and wavelength $\lambda = c/f = 632.8\,nm$. The fluctuation of wavelength is

$$\Delta\lambda = \left|\frac{\partial\lambda}{\partial f}\right|\Delta f = \left|-\frac{\lambda}{f^2}\right|\Delta f \approx 10^{-15} \tag{2.18}$$

therefore, considering constant laser wavelength in our model, we have a relative error of $\Delta\lambda/\lambda \approx 10^{-9}$ that it is acceptable for our applications. For what concern the intensity stability, if we monitor the power of the laser source, we can eliminate its fluctuations.

The second approximation consists in assuming the index of refraction constant and equal for both arm. The index of refraction, one of the most significant parameters of the atmosphere for optical wave propagation, is very sensitive to small-scale temperature fluctuations. In particular, temperature fluctuations combined with turbulent mixing induce a random behavior in the filed of atmospheric index of refraction. A the point $\mathbf{R}$ in the space and time t, the index of refraction can be

mathematically expressed by

$$n(\mathbf{R}, t) = n_0 + \Delta n(\mathbf{R}, t) \tag{2.19}$$

where $n_0 = < n(\mathbf{R}, t) > \approx 1$ is the mean of the index of refraction and $\Delta n(\mathbf{R}, t)$ represent the random deviation, thus $< \Delta n(\mathbf{R}, t) > = 0$. Normalizing the values of $n(\mathbf{R}, t)$ to n_0, fluctuations of the index of refraction are related to corresponding temperature and pressure fluctuations. In particular, the index of refraction for the atmosphere can be written for optical and IR wavelengths as [4]

$$n(R, t) = 1 + 77.6 \cdot 10^{-6}(1 + 7.52 \cdot 10^{-3}\lambda^{-2})\frac{P(R, t)}{T(R, t)} \tag{2.20}$$

where λ is the optical wavelength in μm, P is the pressure in mB, and T is the temperature in Kelvin. According to this expression, then the change in the refraction index can be expressed as

$$
\begin{aligned}
\Delta n(R, t) & = +77.6 \cdot 10^{-6}(1 + 7.52 \cdot 10^{-3}\lambda^{-2})\frac{1}{T(R, t)}\Delta P(R, t) \\
& \quad -1.17 \cdot 10^{-9}\lambda^{-3}\frac{P(R, t)}{T(R, t)}\Delta\lambda - \frac{1}{T^2(R, t)}\Delta T(R, t) \tag{2.21}
\end{aligned}
$$

As it is possible to see from this equation, the wavelength dependence is small for optical frequencies, that is positive since we use laser emitting in the optical and near infrared bands (from $0.4\,\mu m$ up to $1.2\mu m$). Moreover, since the pressure fluctuations are generally negligible, it is easy to see that the refractive index fluctuations associated with the visible and near infrared region of the spectrum are mainly due to random temperature fluctuations (humidity fluctuations only contribute in the far infrared region). Changes in the optical signal due to absorption or scattering by molecule or aerosols are not considered here.

Therefore, as a conclusion, when the interferometer is in vacuum or positioned in a quiet and thermally stabilized environmental place, then, at a first level of approximation, the index of refraction can be considered constant. In figure 2.2 an

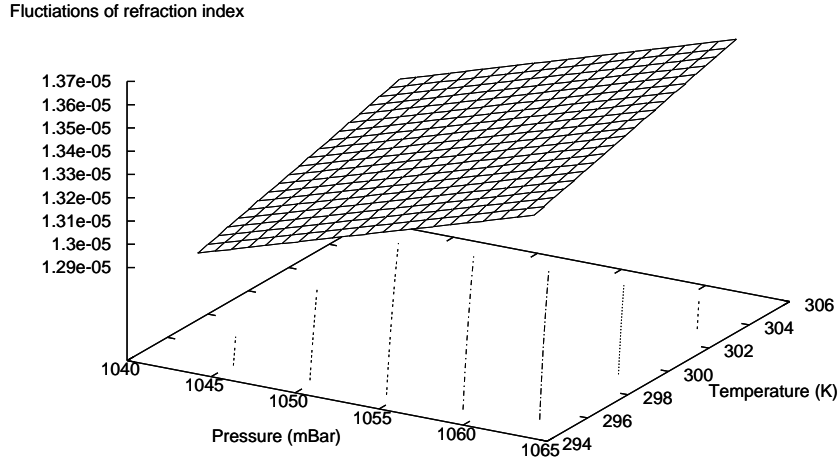example of the variation of refraction index in function of temperature and pressure variation is shown.

Figure 2.2: Variation of index of refraction for $\lambda = 0.5435\,\mu m$.

In the case that a more accurate measure is necessary, we can operate in this way. Define λ_n the wavelength of the laser source in vacuum, and λ_a the laser wavelength in air. So the index of refraction is as

$$n = \frac{\lambda_n}{\lambda_a} \tag{2.22}$$

and we can be defined the wavelength correction number (WCN) as the inverse of the index of refraction. This wavelength correction number can be derived by direct measurement of the index of refraction with a refractometer or by using empirical data. In absence of a refractometer, it is best to measure the air pressure, temperature and relative humidity, and then to relate this data to the refractive index using the semi-empirical formulas obtained by Barrel and Sears [16] and by Edlin [17], for examples:

$$WCN = \frac{1}{n} = \frac{10^6}{N + 10^6} \tag{2.23}$$

36

where

$$N = 0.3836391\,P \cdot \left[\frac{1 + (0.817 - 0.0133\,T)10^6 \cdot P}{1 + 0.0036610\,T} \right] - 3.033 \cdot 10^{-3} \cdot e^{-0.057627T} \cdot H$$

(2.24)

and where the pressure P is measured in $mmHg$, the temperature T in Celsius and the humidity in perceptual %.

For example, assuming standard and homogeneous air composition, a one part-per-million error (ppm) will result from any one of the following condition:

- $1^o\,C$ change in air temperature;

- $2.5\,mm$ of mercury change in the air pressure;

- 80% in relative humidity.

The equation 2.24 gives only an approximation of the refractive index, and thus it has some limitations related to the accuracy of measuring the atmospheric conditions. Generally it is possible to obtain an accuracy of $0.01\,ppm$ using the formula 2.24.

2.2.1 Transfer function estimate

To estimate the transfer function of interferometer, we consider that the seismic wave $s(t)$ is a seismic wave whose propagation vector k lays in the plane in which the sensitive arm $l_2(t)$ of the interferometer is located, as shown in figure 2.3. Therefore, the arrival of a seismic wave along the plane of the interferometer is sensed first by the end mirror S_2 and then, after a delay time t_0, by the mechanical support, hosting the remaining components of the interferometer (beam splitter, mirror S_1, etc.). For simplicity, in our model we consider this mechanical support equivalent to a mass located on the beam splitter position. Of course, due to its structure, the model is symmetric. In fact, the same seismic wave traveling in the opposite direction will
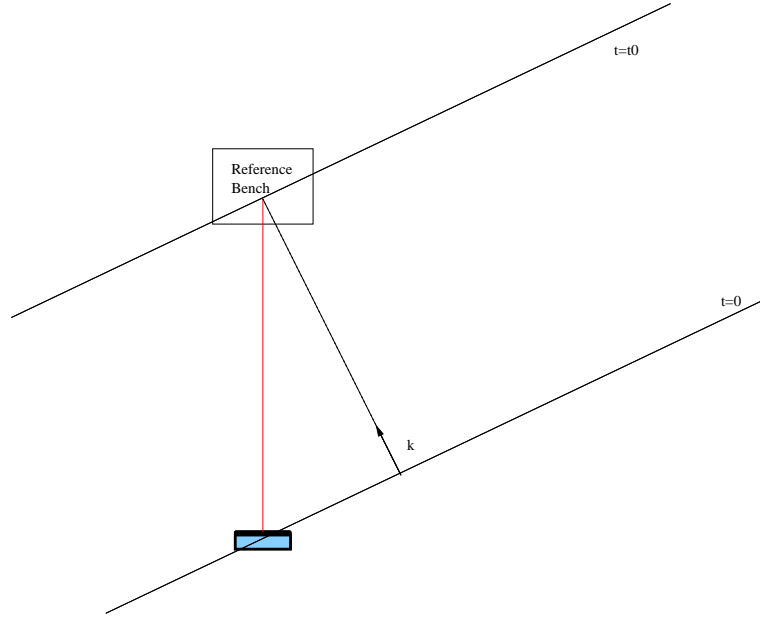
Figure 2.3: Scheme of interferometer response to a seismic wave

be first sensed by the mechanical support, and then, after the same time delay t_0, will be detected by the end mirror, S_2.

Let α be the angle between the wave vector k and the optical axes line l_2, L_2 the position of the mirror S_2, L_b the position of the mirror S_1 respect to the beam splitter and v_s the wave group velocity of signal $s(t)$, then t_0 can be written as

$$t_0 = \frac{[L_2 + g_2(t) + s(t)] \cos \alpha}{v_s} \tag{2.25}$$

where $g_2(t)$ quantifies the residual noise on the mirror S_2, filtered by the mechanical transfer function of the mounting.

For $t > t_0$ the wave front moves both the mirror and the optical length becomes

$$
\begin{aligned}
l_1(t) &= L_b + g_b(t) \\
l_2(t) &= L_2 + g_2(t) + [(s(t) - a_s s(t - t_0)] \cos(\alpha)
\end{aligned}
\tag{2.26}
$$

where a_s is the attenuation factor expressing the ratio of the seismic wave amplitude

at the second mirror with respect to the first one $(0 \leq a_s \leq 1)$. In this way the phase changes as

$$\phi(t) = \frac{4\pi n}{\lambda} \left[L_2 - L_b + g_2(t) - g_b(t) + (s(t) - a_s s(t - t_0)) \cos(\alpha) \right] \tag{2.27}$$

Let $\Delta L(t) = [L_2 - L_b] + g_2(t) - g_b(t)$ be the length change in absence of signal, then the relationship in the Laplace domain between the seismic signal $s(t)$ and the phase is

$$\phi(s) = \frac{4\pi n}{\lambda} \left[\Delta L(s) + S(s) \left(1 - a_s e^{-t_0 s} \right) \cos(\alpha) \right] \tag{2.28}$$

The transfer function of the system that links the input seismic signal $s(t)$ with the output Michelson phase change $\phi(s)$ can be written as

$$H(s) = \frac{\phi(s)}{S(s)} = \frac{4\pi n}{\lambda} \left(1 - a_s e^{-t_0 s} \right) \cos(\alpha) \tag{2.29}$$

while the transfer function for the noise can be written as

$$H_n(s) = \frac{\phi(s)}{\Delta L(s)} = \frac{4\pi n}{\lambda} \tag{2.30}$$

that shows that the interferometer is fully sensitive to all local micronoise (mechanical, refraction index changes, etc.).

Let us now analyze the behavior of the interferometer in the limit of short armlength short compared with the wavelength of the seismic waves. In this case the delay time t_0 becomes small, so that it is possible to expand $e^{-t_0 s}$ in Taylor series as

$$\begin{aligned} H(s) &= \frac{4\pi\, n}{\lambda} \cos(\alpha) \left(1 - a_s \sum_{k=0}^{\infty} \frac{s^k}{k!} \left. \frac{d^k e^{-t_0 s}}{ds^k} \right|_{t_0=0} \right) \\ &= \frac{4\pi\, n}{\lambda} \cos(\alpha) \left((1 - a_s) + a_s \sum_{k=1}^{\infty} \frac{s^k}{k!} \left. \frac{d^k e^{-t_0 s}}{ds^k} \right|_{t_0=0} \right) \end{aligned} \tag{2.31}$$

And since we are considering an interferometer with short arms, we can retain only the term for $k = 1$ of Taylor series and it is possible to consider that the attenuation factor $a_s = 1$. In this way we obtain the relation between the input seismic signal

$s(t)$ with the output Michelson phase change $\phi(t)$ can be written in the Laplace domain as

$$\phi(s) = \frac{4\pi n}{\lambda} \cos(\alpha) t_0 s S(s) \tag{2.32}$$

and then in the time domain as

$$\phi(t) = \frac{4\pi n}{\lambda} \cos(\alpha) t_0 \left(U(t - t_0) \frac{ds(t)}{dt} \right) \tag{2.33}$$

This means that according to the above hypothesis the interferometer phase is proportional to the input signal derivate at least at the first order, and therefore to the velocity of the seismic waves.

Here, in order to provide a clearer and simpler analysis we report the harmonic response of the interferometer to seismic signals whose wavelengths are much larger than the interferometer arm-lengths. Using the t_0 explicit form, the harmonic response is

$$H(j\omega) = \frac{4\pi n}{\lambda v_s(j\omega)} j\omega \cos^2(\alpha) \tag{2.34}$$

where $v_s(j\omega)$ is the velocity of seismic wave at angular frequency ω.

In order to show the angular dependence of the instrument sensitivity, we plotted the sensitivity diagram according to equation 2.34 (see figure 2.4). In can be easily seen that this diagram has the classical shape of a dipole, in which the maximum sensitivity is for $\alpha = 0$ and $\alpha = \pi$ and the minimum sensitivity is for $\alpha = \pi/2$ and $\alpha = 3\pi/2$. According to this diagram it is easy also to see that it is possible to build an omnidirectional interferometric instrument to measure seismic noise, by simply using the Michelson interferometers oriented perpendicularly each other. In fact, with interferometers with equal armlengths and with optics having the same characteristics, is possible to build an instrument able to detect seismic waves with no angular dependence.

The only remaining point is how to extract the function $\phi(t)$ by the measurement of the interferometer intensity through the output photodiode. For this task it is
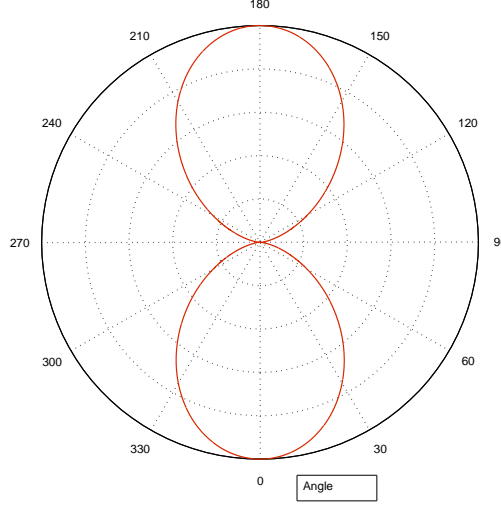
Figure 2.4: Normalized sensitivity diagram for a Michelson interferometer with free mirror in the $0\,rad$ direction.

necessary the inversion of the equation 2.12 to obtain

$$\phi(t) = \cos^{-1}\left[2\frac{I(t) - I_{min}}{I_{max} - I_{min}} - 1\right] \tag{2.35}$$

Particular care is needed in the application of this formula. In fact, if during the selected time interval the output intensity of the interferometer reaches its maximum or minimum value, then the equation 2.35 is not longer valid due to the periodicity of the cosine function. Physically, it means that the interferometer is passing from the working fringe to the next one. The method used to solve this problem is presented in the section 2.3. At this point it is enough to derive numerically the equation 2.33 to obtain the acceleration of free mirror respect to the reference bench:

$$a(t) = \frac{d^2 s(t)}{dt^2} = \frac{\lambda}{4\pi n t_o \cos(\alpha)}\dot{\phi}(t) \tag{2.36}$$

41

2.2.2 Error in Taylor expansion

The equation 2.33 has been written considering only the first term of the Taylor series. In order to evaluate the instrument sensitivity it is important to consider the error in the Taylor series truncation.

Consider the formula of the rest of the Taylor series:

$$R_n(t_0) = \int_0^{t_0} f^{(n+1)}(t) \frac{(t-t_0)^n}{n!} dt$$

If we retain only the first term in the Taylor series, we make an error

$$R_2 = \left\| \frac{3\pi^2 f^2 L^4}{v_s^4} \right\| \tag{2.37}$$

For our prototype, in which $L = 0.2$, and for several wave velocities we make an error in function of the seismic wave frequency illustrated in figure 2.5:
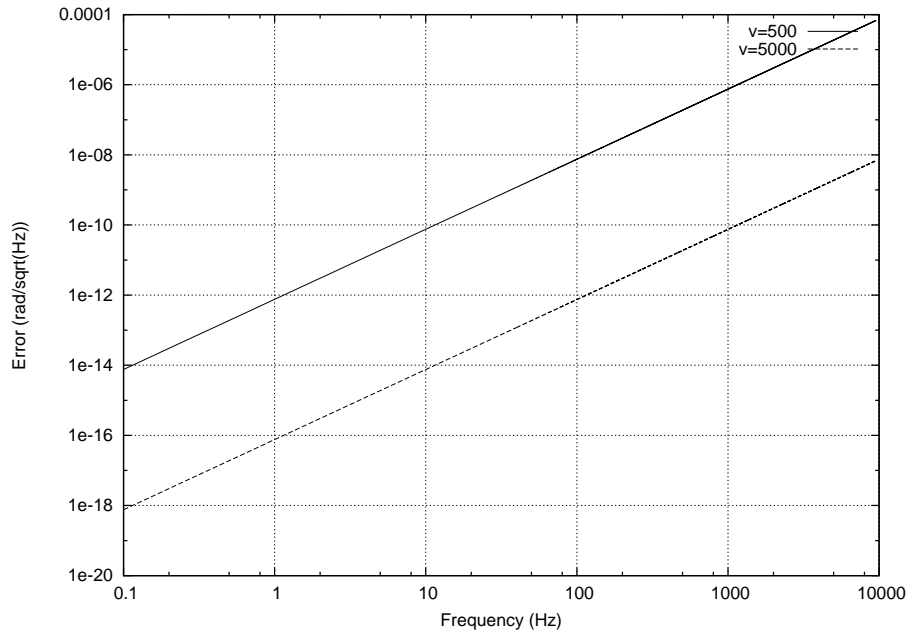
Figure 2.5: Phase error due to Taylor series truncation.

2.2.3   Optimum fringe geometry

Controlling fringe geometry is necessary for basic operation of the interferometer as well as maximizing the signal to noise ratio. This is accomplished by properly offsetting, magnifying, and directing the laser beam in the arms, before they reach the photodiodes. The component of the interferometer, for example the separation distance d of the two beam, can be controlled to produce an optimum fringe pattern at the photodiodes.

Maximum visibility

In interferometry, the *visibility* is usually defined as the ratio of the maximum measured signal and the minimum, as shown in equation 2.10. In this paragraph the visibility is defined as the difference between the maximum and the minimum, not the ratio. This difference becomes a voltage difference at the photodiode outputs and will be compared to the background electronic noise for a signal to noise ratio calculation.

Consider a laser source with wavelength λ, the width of a fringe $\delta = \lambda/2$ and the photodiode sensor size l can be optimized to give the greatest visibility. Consider a sensor of width l centered on fringe pattern as depicted in figure 2.6. The cylindrical lens expands the laser beam for matching the diode sensor area. It is assumed that the beam width, b is much greater then the beam separation distance, d. The maximum integrated intensity measurement will occur when the sensor is centered on the bright region of the spatially harmonic intensity distribution, $I(\xi)$, which is given by

$$I(\xi) = \frac{P}{2b}\left(1 + \cos\left(\frac{2\xi\pi}{\delta}\right)\right) \tag{2.38}$$

where P is the total power of the combined beams, ξ is the location along the fringe pattern. The intensity distribution for two interfering, circular cross section beams

43
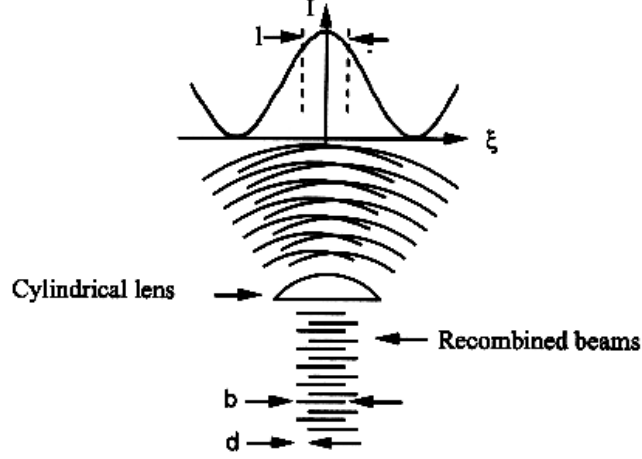
Figure 2.6: Diode fringe pattern.

with a Gaussian intensity distribution is more complicated then equation 2.38, but is not necessary for this analysis.

Integrating equation 2.38 over the length of the sensor l gives the maximum integrated intensity measurement:

$$S_{max} = \frac{P}{2b} \int_0^l \left(1 + \cos \frac{2\xi\pi}{\delta}\right) d\xi = \frac{P}{2b} \left(l + \frac{\delta}{2\pi} \sin \frac{\pi l}{\delta}\right) \qquad (2.39)$$

Similarly, for the minimum integrated intensity measurement is centered on a dark part of the fringe pattern:

$$S_{min} = \frac{P}{2b} \int_0^l \left(1 - \cos \frac{2\xi\pi}{\delta}\right) d\xi = \frac{P}{2b} \left(l - \frac{\delta}{2\pi} \sin \frac{\pi l}{\delta}\right) \qquad (2.40)$$

Differencing S_{max} and S_{min} gives an expression for the visibility:

$$V = S_{max} - S_{min} = \frac{P}{b} \left(\frac{\delta}{\pi} \sin \frac{\pi l}{\delta}\right) \qquad (2.41)$$

It is now clear that the optimum relationship between fringe width δ and the photodiode sensor size l is

$$l = \frac{\delta}{2} \qquad (2.42)$$

44

that gives a maximum visibility of

$$V_{max} = \frac{P\delta}{b\pi} \qquad (2.43)$$

Beam separation distance

The fringe pattern intensity will have an harmonic spatial distribution similar to figure 2.6. The fringe pattern can be predicted by treating each laser beam as a diverged spherical wavefront. The fringe width δ is

$$\delta = \frac{\lambda R}{d} \qquad (2.44)$$

where R is the radius of curvature of the wavefront of the laser beam. The beam width b is given by

$$b = R\phi \qquad (2.45)$$

where ϕ is the laser beam divergence angle. Combining equation 2.43, 2.44 and 2.45 gives an expression for the maximum visibility:

$$V_{max} = \frac{P\lambda}{\phi\pi d} \qquad (2.46)$$

Equation 2.46 predicts that decreasing d (increasing the fringe width) yields better visibility. d can be made arbitrarily small but the sensed portion of the interference pattern l can be no larger than the width of the entire interference pattern, which is of course limited to the beam width b. Further, there is a more practical upper bound on δ, and thus on l. Recall that at least 1/4 cycle ($\delta/4$) of an intensity distribution is needed to allow proper placement of the diodes and this is the actually the required distance between center locations of the photodiode. Considering now that the photodiode is to have a width of $\delta/2$, the fringe pattern must now contain at least 3/4 of a cycle of fringes, or $3\delta/4$. If the beam of width b are offset by a distance d, the size of the interferometer region will have a width

$b - d$. This gives, using equation 2.44 and 2.45,

$$b - d = \frac{3}{4}\delta = \frac{3}{4}\left(\frac{\lambda b}{\phi d}\right) \tag{2.47}$$

Solving for d after neglecting the second order term:

$$d = \frac{3}{4}\left(\frac{\lambda}{\phi}\right) \tag{2.48}$$

For example, for a Helium-Neon laser with $\phi = 1.6\,mrad$

$$d = \frac{3}{4}\left(\frac{632.8\,nm}{1.6\,mrad}\right) = 0.39\,mm \tag{2.49}$$

This magnitude of position is easily achieved with optical translation stages. A larger separation distance will produce more fringes with smaller fringe width δ. The equation 2.46 shows that the signal strength will decrease proportionally.

Fringe pattern magnification

The interference region will most likely need to be magnified to accommodate the size of the photodiode. The interference region should be 3/4 of the fringe width and the sensor should be 1/2 of the fringe width, which means the interferometer region should be 3/2 of the width of the photodiode. In our experiment, the photodiodes were about $5\,mm$ wide squares. This required a magnification factor of about 4. The magnification is done with a cylindrical lens so that the fringes are made wider then the photodiode but not taller. This utilizes all the available light for better signal to noise ratio.

2.2.4 Sampling frequency choice

To choose the sampling frequency F_c it is important to consider that the sampling frequency must be at least two times the maximum frequency of the acquired signal

$I(t)$ (Nyquist theorem). Thus the sampling frequency F_c should be higher than $\dot{\phi}(t)/\pi$, where $\dot{\phi}(t)$ is the velocity of the phase.

Remember that

$$\phi(t) = \frac{4\pi n t_0}{\lambda} \frac{ds(t)}{dt} \tag{2.50}$$

and that the propagation time $t_0 = L/v_s$, the instantaneous frequency of $I(t)$ is

$$f(t) = \frac{\dot{\phi}}{2\pi} = \frac{2nL}{\lambda v_s} \frac{d^2 s(t)}{dt^2} \tag{2.51}$$

Then it is possible to choose the sampling frequency considering the maximum acceleration a_p that the instrument can measure. In fact the sampling frequency is related to the phase derivative by the relation

$$F_c > 2 f_{max} = \frac{\dot{\phi}}{\pi} \tag{2.52}$$

and so we are able to determine the minimum sampling frequency in function of the instrument parameters as

$$F_c > \frac{4nL}{\lambda v_m} a_p \tag{2.53}$$

where the peak acceleration a_p is a calibration parameter and v_m is the minimum wave velocity attended. For example, for our prototype in which $L = 0.2$, if we choose the sampling frequency following the graph of figure 2.7.

2.3 Signal reconstruction

As we have seen, from equation 2.35 we are not able to reconstruct the phase $\phi(t)$ without ambiguity because of the periodicity of the function cosine. To avoid this problem there are a lot of algorithms. We use the algorithm shown in the next paragraph (2.3.1). To apply this algorithm two signals are necessary, the first one proportional to the sine of the phase, and the last one proportional to the cosine of the phase. To obtain these signals we propose the techniques, shown in paragraph 2.3.2 and 2.3.3 .
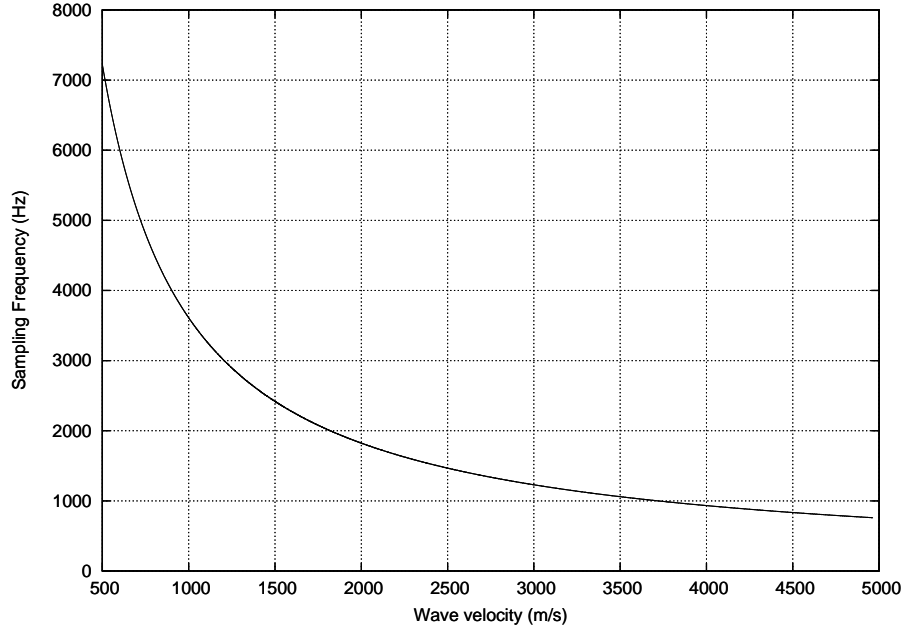
Figure 2.7: Minimum sampling frequency in function of minimum seismic wave velocity for $a_p = g/4$.

2.3.1 Phase-unwrapping algorithm

Suppose that we have two signals in quadrature, $V_1(t)$ and $V_2(t)$, proportional to the sine and the cosine of the phase ϕ, respectively. Both signals are equidistantly sampled with the sampling periods $T = t_{i+1} - t_i$, given a series of measurement values $V_1(t_i)$ and $V_2(t_i)$. The observation period is defined from $i = 1 \ldots n$.

In the first step a *quadrature error correction* is necessary. In fact if we make a parametric plot of the interferometer signal and the lockin signal, the orbit defined by the Lissajous pattern will not be perfectly circular for several reasons. Misalignment of the beams will reduce the amount of the light captured by the detector; offsets and gains of the amplifier used for the signal conditioner, and principally the two signal are not perfectly in quadrature. Uncorrected, the ellipticity causes significant errors if trying to estimate displacements of only a fraction of wave length.

In this case the phase difference ϕ_0 is not exactly $\pi/2$ and an error in calculating

the position arises. This error can be corrected, but since it is not cumulative, and repeats every time the path length changes by the laser wavelength λ, this correction is only needed when the motion on scale much less then λ are important. For a phase misalignment of ϕ_0, the two signal in quadrature can be represented (after it has been normalized) as

$$
\begin{aligned}
V_1 &= \sin(\phi(t) + \phi_0) \\
V_2 &= \cos(\phi(t))
\end{aligned}
\tag{2.54}
$$

For a given set of measurements, equations 2.54 contain two unknown: $\phi(t)$ and ϕ_0. An equation can be written involving only V_1, V_2 and ϕ_0:

$$
V_2^2 = \frac{\left[\cos\left(\arctan\left(\frac{V_1/V_2 - \sin\phi_0}{\cos\phi_0}\right)\right)\right]^2 + \left[\sin\left(\arctan\left(\frac{V_1/V_2 - \sin\phi_0}{\cos\phi_0} + \phi_0\right)\right)\right]^2}{1 + \left(\frac{V_1}{V_2}\right)}
\tag{2.55}
$$

Section of data are used to curve fit for ϕ_0. Once a value for ϕ_0 is found, all the V_1 data can be corrected to represent a diode measurement with $\phi_0 = 0$. Equations 2.54 can be used to solve for actual $\phi(t)$

$$
\phi(t) = \arctan\left(\frac{V_1/V_2 - \sin(\phi_0)}{\cos\phi_0}\right)
\tag{2.56}
$$

After the quadrature error correction procedure, $\phi_0 = 0$ and the corresponding values of the phase of motion $\phi(t)$ at t_i is determined as follow:

$$
\phi(t_i) = \arctan\frac{V_1(t_i)}{V_2(t_i)} + m\pi, \qquad \text{with } m = 0, 1, 2, \ldots
\tag{2.57}
$$

An integer number m is chosen to avoid discontinuities of $\phi(t_i)$. To determine m and $\phi(t_i)$, we must find the discontinuities of the arctangent term in equation 2.57 and determine whether to add to, or subtract from, m. Figure 2.8 gives a scheme of the algorithm.

In step I, the adjacent values are compared. If the difference between the two values is greater that $\pi/2$, we infer a discontinuity and it reveals that there is a
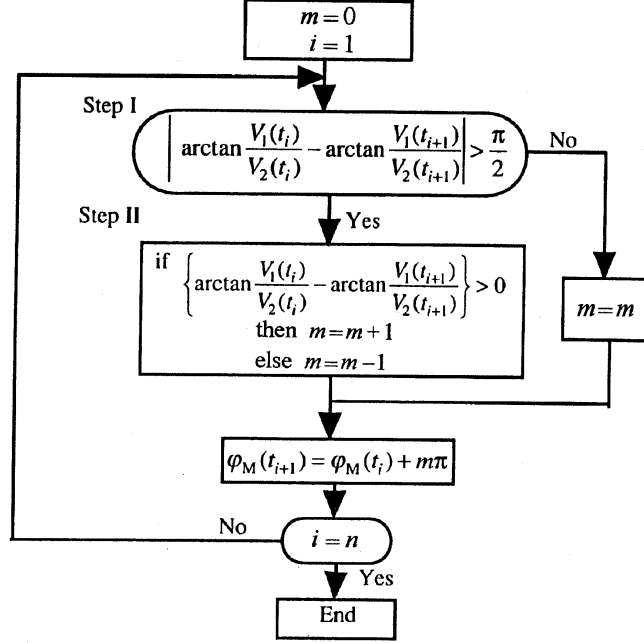
Figure 2.8: Algorithm of the phase-unwrapping process.

changing of the fringe. In the step II, the direction of the discontinuity is determined by the slope of the adjacent values and 1 is added to or subtracted from m, depending on the direction.

2.3.2 Modulation technique

The modulation technique consists in changing the optical length of an interferometer arm as

$$l_m(t) = l_{m_c} cos(\omega_m t) \qquad (2.58)$$

where l_{m_c} is the modulation amplitude and $f_c = 2\pi/\omega_m$ is the modulation amplitude. Then the intensity measured by the photodiode is

$$I(t) = I_{min} + \frac{I_{max} + I_{min}}{2} \left\{ 1 + \cos \left[\frac{4\pi n}{\lambda} \left(l_{eq}(t) + l_{m_c} cos(\omega_m t) \right) \right] \right\} \qquad (2.59)$$

50

where $l_{eq}(t)$ is the equivalent displacement of the free mirror. With a lot of algebra we obtain

$$
\begin{aligned}
I(t) \;=\; & I_{min} + \frac{I_{max} - I_{min}}{2} \left\{ 1 + \cos\left(\frac{4\pi n}{\lambda} l_{eq}(t)\right) \cos\left(\frac{4\pi n}{\lambda} m \cos(\omega_m t)\right) + \right. \\
& \left. - \sin\left(\frac{4\pi n}{\lambda} l_{eq}(t)\right) \sin\left(\frac{4\pi n}{\lambda} m \cos(\omega_m t)\right) \right\} \longrightarrow \\
I(t) \;=\; & \frac{I_{max} + I_{min}}{2} + \frac{I_{max} - I_{min}}{2} \cos\left(\frac{4\pi n}{\lambda} l_{eq}(t)\right) \cos\left(\frac{4\pi n}{\lambda} m \cos(\omega_m t)\right) + \\
& - \frac{I_{max} - I_{min}}{2} \sin\left(\frac{4\pi n}{\lambda} l_{eq}(t)\right) \sin\left(\frac{4\pi n}{\lambda} m \cos(\omega_m t)\right) \qquad (2.60)
\end{aligned}
$$

Considering the Bessel series

$$
\begin{aligned}
\cos(z\cos(\theta)) \;&=\; J_0(z) + 2\sum_{k=1}^{+\infty} (-1)^k J_{2k}(z) \cos(2k\theta) \\
\sin(z\cos(\theta)) \;&=\; 2\sum_{k=0}^{+\infty} (-1)^k J_{2k+1}(z) \cos((2k+1)\theta) \qquad (2.61)
\end{aligned}
$$

it is possible to expand the equation 2.60 in series as

$$
\begin{aligned}
I(t) \;=\; & \left(\frac{I_{max} + I_{min}}{2}\right) + \left(\frac{I_{max} - I_{min}}{2}\right) \cos\left[\frac{4\pi n}{\lambda} l_{eq}(t)\right] \cdot \\
& \left[J_0\left(\frac{4\pi n}{\lambda} l_{m_c}\right) + 2\sum_{k=1}^{+\infty} (-1)^k J_{2k}\left(\frac{4\pi n}{\lambda} l_{m_c}\right) \cos(2k\omega_m t) \right] + \\
& - \left(\frac{I_{max} - I_{min}}{2}\right) \sin\left[\frac{4\pi n}{\lambda} l_{eq}(t)\right] \cdot \\
& \left[2\sum_{k=0}^{+\infty} (-1)^k J_{2k+1}\left(\frac{4\pi n}{\lambda} l_{m_c}\right) \cos[(2k+1)\omega_m t] \right] \qquad (2.62)
\end{aligned}
$$

The equation 2.62 shows that the output signal is composed by the sum of harmonics of the modulation frequency with amplitude depending by the mirror displacement $l_{eq}(t)$ and by the modulation amplitude l_{m_c}.

If we choose the modulation amplitude $l_{m_c} \ll \lambda$ it is possible to consider only the term J_0 and J_1 of the Bessel series to obtain

$$
I(t) \;\simeq\; \left(\frac{I_{max} + I_{min}}{2}\right) + \left(\frac{I_{max} - I_{min}}{2}\right) \cos\left(\frac{4\pi n}{\lambda} l_{eq}(t)\right) J_0\left(\frac{4\pi n}{\lambda} l_{m_c}\right) +
$$

$$- \left(\frac{I_{max} - I_{min}}{2} \right) \sin \left(\frac{4\pi n}{\lambda} l_{eq}(t) \right) 2 J_1 \left(\frac{4\pi n}{\lambda} l_{m_c} \right) \cos(\omega_m t) \qquad (2.63)$$

To obtain a signal proportional to the cosine of the mirror displacement $l_{eq}(t)$, we filter the signal $I(t)$ with a low pass filter with cutoff frequency equal to the maximum frequency expected of $l_{eq}(t)$ and less than the modulation frequency. The last step is to subtract the mean of $I(t)$ to obtain

$$V_2(t) = \left(\frac{I_{max} - I_{min}}{2} \right) J_0 \left(\frac{4\pi n}{\lambda} l_{m_c} \right) \cos \left(\frac{4\pi n}{\lambda} l_{eq}(t) \right) \qquad (2.64)$$

To obtain a signal proportional to the sine of mirror displacement $l_{eq}(t)$, we can use the synchronous demodulation technique. This procedure can be realized using a lockin amplifier, which schema is shown in figure 2.9.
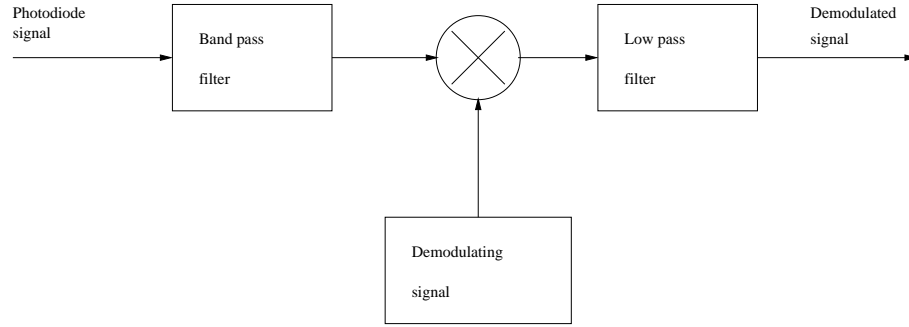
Figure 2.9: Block scheme of a lockin amplifier.

The lockin amplifier works according to the following steps:

1. to increase the signal to noise ratio, the output of the photodiode is filtered with a pass band filter with center frequency equal to the modulation frequency $\omega_m/2\pi$ and with pass band equal to the frequency band of $l_{eq}(t)$. In this way we obtain the signal

$$\hat{I}(t) = - \left(\frac{I_{max} - I_{min}}{2} \right) \sin \left(\frac{4\pi n}{\lambda} l_{eq}(t) \right) 2 J_1 \left(\frac{4\pi n}{\lambda} l_{m_c} \right) \cos(\omega_m t) \qquad (2.65)$$

2. it multiplies this signal with a sinusoidal with the same frequency and the same phase of the modulation signal, to obtain the signal

$$\hat{I}(t) = -\left(\frac{I_{max} - I_{min}}{2}\right) \sin\left(\frac{4\pi n}{\lambda} l_{eq}(t)\right) 2J_1\left(\frac{4\pi n}{\lambda} l_{m_c}\right)(1 - \sin^2(\omega_m t))$$

(2.66)

3. it uses a low pass filter to obtain the signal

$$V_1(t) = -\left(\frac{I_{max} - I_{min}}{2}\right) \sin\left(\frac{4\pi n}{\lambda} l_{eq}(t)\right) 2J_1\left(\frac{4\pi n}{\lambda} l_{m_c}\right)$$

(2.67)

In this way it is possible to obtain two signal in quadrature to use the phase-unwrapping algorithm.

2.3.3 The quadrature laser interferometer

The quadrature interferometer uses a polarized laser, two photodiodes and an optical trick. The laser is oriented so the polarization axis is rotated $\pi/4$ radians with respect to the alignment of the beam splitter and reference mirror, as shown in figure 2.10. The one polarized beam oriented at this angle is vectorially equivalent
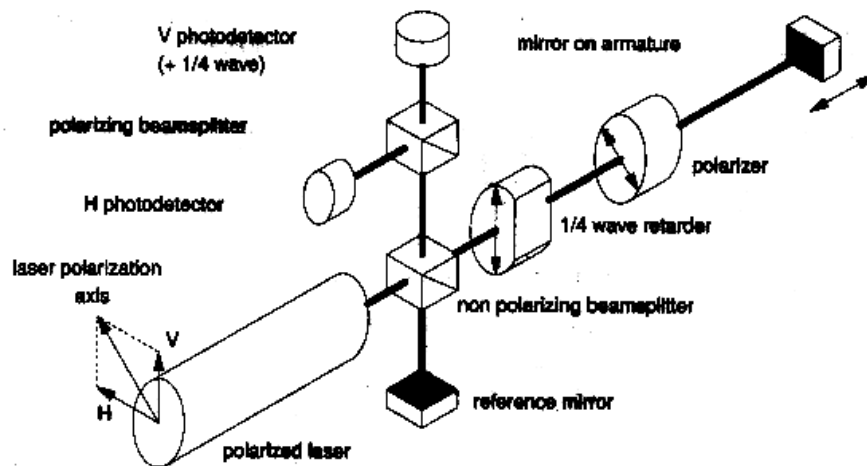
Figure 2.10: Exploted view of a quadrature laser interferometer.

to two beam of equal intensity occupying the same space, designed with V and H, one polarized vertically and one polarized horizontally. The two beam are ultimately separated with a polarized beam splitter, and using a photodiode for each beam, two interferometer are created from these components.

The trick is provided by a polarized device called 1/4 wave retarder, which is designed to slow light polarized in its axis more than the light polarized perpendicular to its axis. Its axis is placed in parallel with the polarization of beam "V", effectively adding 1/4 wavelength of its path. That photodiodes' output will always differ by 1/4 of a fringe, or $\pi/2$ from each other, so the beams in the two arms are in quadrature.

With a single detector the determination of the displacement is very difficult, since the variation of the photodiode output is severely dependent on the average position of the mirror. In fact, best photodiodes resolution occurs in the middle of the fringe, in which the change of the light intensity as a function of the mirror position is at a maximum. Poorest resolution occurs when the average mirror position causes intensity extrema (dark and fringe) whether from maximal constructive or destructive interference between the beams.

For vibration amplitudes smaller than the wavelength, intensity variation around the minimum (or maximum) of intensity would be very small. In such an unfortunate condition, it would be useful to be able to reposition one of the mirrors to change the path length of 1/4 wavelength, so that the photodiodes would have maximum sensitivity, as in the middle fringe. The quadrature laser effectively solves the problem by using two interferometers, one of which has a path length 1/4 wavelength longer than other, so one is always near the point of maximal sensitivity.

Chapter 3

Implemented Prototype

The experimental apparatus used as prototype for a laser interferometry based seismic sensor consists mainly of a Michelson interferometer in air, an accelerometer for comparison, a digital acquisition system to get data from these instruments and to store them in an electronic archive. A triaxial episensor (model FBA ES-T, from Kinemetrics) is located close to the interferometer to monitor the acceleration in that point. The episensor is made of three independent accelerometers oriented in the different directions of the space. In this way the probe can measure the accelerations along the three spatial axis: x, y and z. The user selectable full scale of all the accelerometers was chosen at $\pm g/4$, where $g = 9.806 m/s^2$ is the standard gravitational acceleration while the voltage output level is fixed at $20\,V$. In this configuration the instrumental sensitivity is $\pm 80\,V/g$. The band nominally spans from DC to $200 Hz$, while the nominal dynamic range is $155 dB$, according to the instrument specifications.

3.1 The optical setup

A scheme of the implemented interferometer test system is shown in figure 3.1. The light beam coming from the laser is sent to a first beam-splitter. The deviated beam is sent to a photodiode 1 used to monitor the light source power, while the transmitted one is split again by the second beam-splitter and, after the reflection of the two resulting beams on the end mirrors 1 and 2, is finally recombined on the interferometer output photodiode 2. The arm-lengths of the interferometer are about $20\,cm$. An optical isolator, located between the laser and the first beam-splitter, prevents the backscattering of light toward the laser source. A phase modulator is placed along the fixed arm. All the optical elements of the interferometer are fixed to an optical bench with $30\,cm$ of height and $60\,cm$ of width. In the following subsections the characteristics of the optical components are shown.
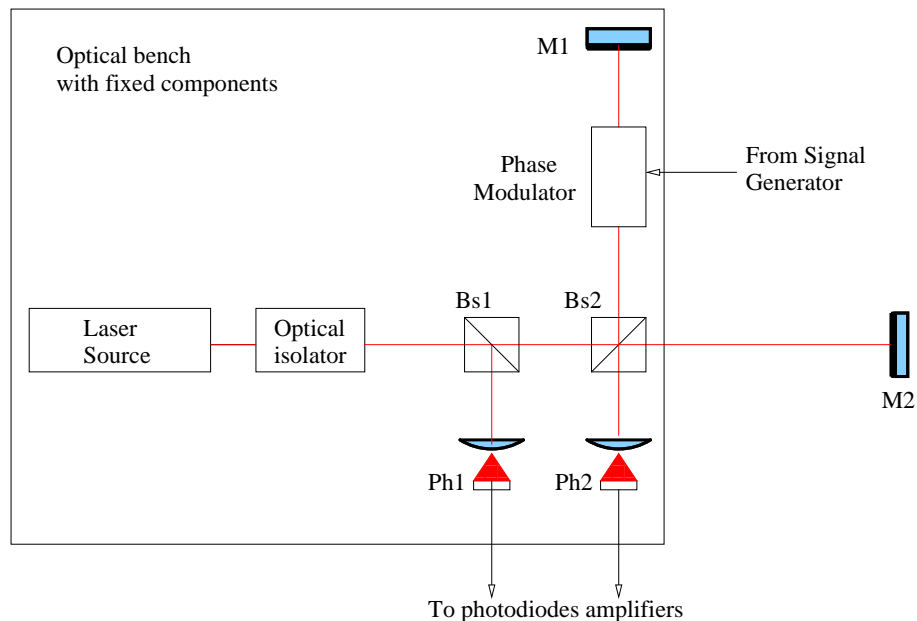
Figure 3.1: Optical setup of our prototype (not in scale).

The Laser

The laser used in the prototype is a Helium-Neon laser, model 25-LGP-173 of Mells-Griot© with the specifications shown in table 3.1. It has been chosen because it guarantees a good frequency stability at a low cost. In figure 3.2 the power spectral density of the amplitude laser noise is shown. As can be seen, these fluctuations are relevant particularly in the frequency band $f < 1\,Hz$ while the resonances at high frequency are due to the photodiode noise. If we want a better frequency or intensity stability it is possible to use a stabilized laser source.

Optical characteristics
Output Wavelength: $543.5\,nm$
Output Power: $0.3\,mW$
Mode: TEM00
Mode Spacing: $373\,MHz$
Beam Dimension $(1/e^2)$: $0.79\,mm$
Far-Field Divergence $(1/e^2)$: $0.88\,mrad$
Polarization: Linear
Maximum Mode Sweeping: 5%
Long-Term Drift: $\pm2\%$
Noise Range: $30\,Hz \pm 10\,MHz$
Noise: $< 0.5\%$ rms

Table 3.1: Laser characteristics.

The Optical isolator

The optical isolators are used to reduce or eliminate the effects of optical feedback, reflections of the laser's own energy back into itself. The effects of optical feedback are well known: amplitude fluctuation, frequency shift, limitation of modulation

bandwidth, noise and even damage. Much like a diode in an electrical circuit, the isolator transmits light in one direction only. An isolator consists of a Faraday rotator, two polarizers and a body to house the parts. The Faraday rotator consists of a magneto-optic material contained in a magnetic field.

The optical isolator is based on the Faraday effect: the plane of polarized light rotates while transmitting through glass (or other material) that is contained in a magnetic field; the direction of rotation is dependent on the direction of the magnetic field, and not on the direction of light propagation (non-reciprocal). The amount of rotation is $Q = VLH$, where:

- V is the Verdet constant, a property of the optical material; it is important to note that the Verdet Constant is wavelength-dependent.

- L is the path length through the optical material in centimeters.

- H is the magnetic field strength in Oersted.
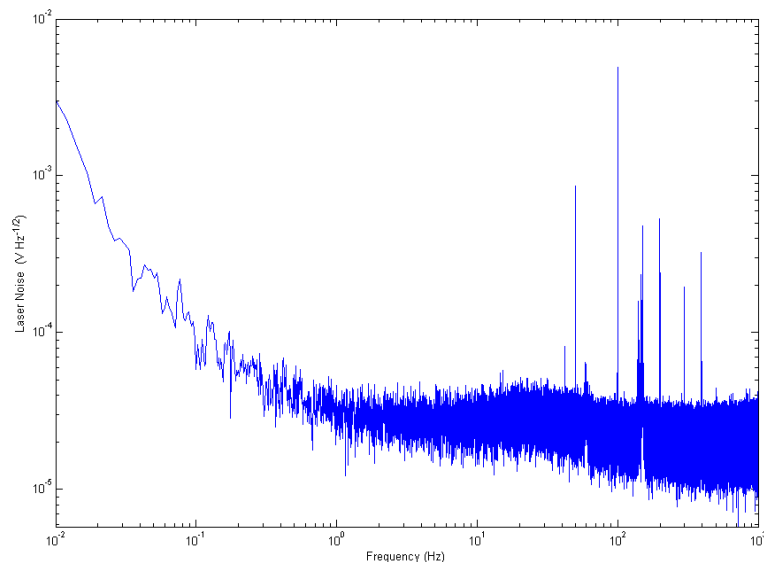
Figure 3.2: Power spectral density of the amplitude laser noise.

Laser light, whether or not polarized, enters the input polarizer and becomes linearly polarized, say in the vertical plane (0°). It then enters the Faraday rotator, designed to rotate the plane of polarization by 45°, say in the clockwise sense. It then exits through the output polarizer whose axis is at 45° (see top part of figure 3.3). The light leaves the isolator, and reflections occur. This reflected light constitutes feedback. This feedback re-enters the isolator, back through the output polarizer where it is re-polarized at 45°. It then passes back through the rotator and is further rotated by another 45°, still in the clockwise sense, making a total of 90° with respect to the input polarizer (0°). It is seen that the light is extinguished here (see bottom part of figure 3.3). Thus, we have succeeded in isolating the laser from its own reflections.
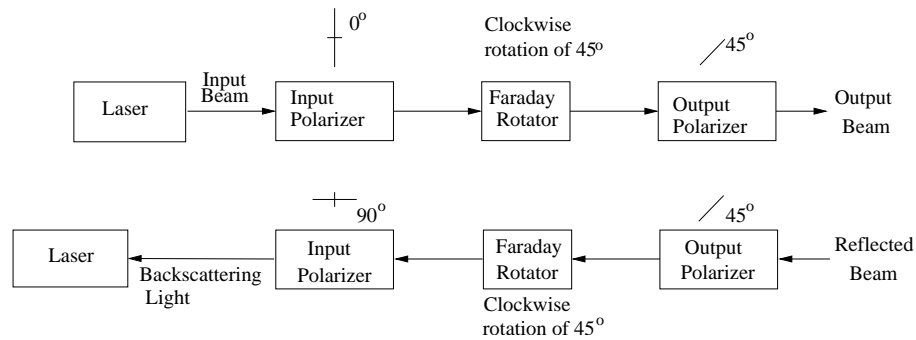
Figure 3.3: Optical isolator effect on input laser beam (top) and on the reflected laser beam (bottom).

In a correctly adjusted isolator, maximum isolation and transmission occur together when the axis of the input polarizer is parallel to the plane of the polarized laser, and the output polarizer is at 45°. If the wavelength changes, then rotation is no longer 45°, and both isolation and transmission will decrease. Thus, it is desirable to readjust the isolator if the wavelength changes.

The optical isolator used in the our prototype is a OFR©, model IO-3-λ-LP, having the following characteristics:

Aperture	Laser wavelength	Transmission	Isolation
$3.0\,mm$	$505 \pm 700\,nm$	$> 93\%$	$35 \pm 40\,dB$

Mirrors and beam splitters

The mirrors are broadband metallic mirrors, model 05B10ER.1 of the Newport©, with enhanced aluminum coating and Pyrex© substratum. Pyrex© is chosen because it has very low thermal expansion. The multilayer dielectric stack deposited over the aluminum film boosts reflectance and improves the durability of the coating. The average reflectivity is greater then 93% in the visible range.

The beam splitters are laser line non-polarizing cube beam splitters, model 05BC16NP of the Newport©. They provide true 50/50 beamsplitting without altering the beam polarization. These beamsplitters consist of a pair of precision right-angle prisms carefully cemented together to minimize wavefront distortion. The hypotenuse of one of the prisms is coated with a multilayer all-dielectric non polarizing beamsplitter coating optimized for a specific laser line. The four faces are antireflected coated with a multilayer dielectric coating to minimize surface reflection losses at the laser lines. The specifics are: a waveform distortion $< \lambda/4$, a transmission and a reflection coefficient of $50\% \pm 3\%$ and a deviation of the transmission or of the reflection beam $< 5\,arcmin$.

The phase modulator

Electro-optic modulators allow you to control the amplitude, the phase and the polarization state of an optical beam electrically. They are made out of discrete pieces of nonlinear optical crystal and they are based on electro-optic effect.

The electro-optic effect in a crystal is the change in the refractive index that is proportional to the magnitude of an external applied electric field. In particular,

the induced refractive index change caused by an external electric field is

$$\Delta n = \frac{1}{2} n_e^2 r_{ij} E \qquad (3.1)$$

where Δn is the change in the index of refraction, n_e is the unperturbed index of refraction, r_{33} is the appropriate element in the third-rank electro-optic tensor describing the optical proprieties of the crystal, and E is the applied electric field.

The most common crystal, used in the amplitude and phase modulators, are of lithium tantalate, or Magnesium oxide-doped lithium niobate. These crystals are grown in large, low scatter-loss boules, and have a wide transparency window. They are also nonhygroscopyc so they can be left in use for indefinite periods without being in a sealed enclosure.

The phase modulator is the simplest electro-optic modulator. An electric field is applied along one of the crystal's principal axes. Light polarized along any other principal axis experiences an index of refraction change, hence an optical path length change, that is proportional to the applied electric field.

Thus the phase of the optical field exiting from the crystal therefore depends on the applied electric field. The most common phase modulator is the transverse modulator, as shown in figure 3.4, which consists of an electro-optic crystal between parallel electrodes.

These modulators develop large electric field between the electrodes while simultaneously providing a long interaction length l in which to accumulate phase shift. The optical phase shift $\Delta\phi$ obtained from applying a voltage V between the electrodes is given by

$$\Delta\phi = \frac{2\pi}{\lambda} \left(\frac{n_e^3 r_{33}}{2} \right) \frac{l}{d} V \qquad (3.2)$$

where λ is the laser wavelength and d is the electrode separation.

A commonly used figure of merit for electro-optics modulators is the *half-wave voltage* V_π. It is defined as the voltage required to produce an electro-optic phase
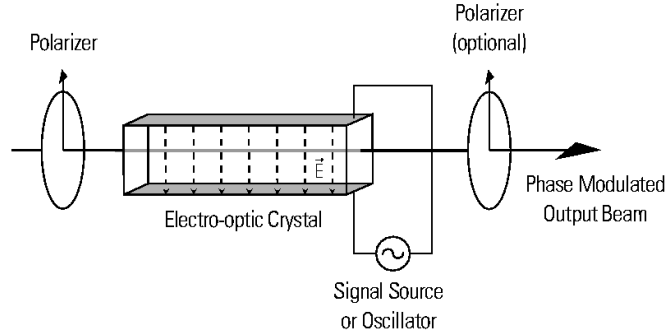
Figure 3.4: Scheme of phase modulator.

shift of π. Substituting in the equation 3.2 yields

$$V_\pi = \frac{\lambda d}{n_e^3 r_{33} l} \qquad (3.3)$$

For a broadband phase modulation and for a laser emitting at $\lambda = 543.5\,nm$ (green), V_π is typically $105\,V$, corresponding to a modulation depth of $0.03\,rad/V$. Note that at other wavelength these values change proportionally.

The photodiodes

The photodiodes used in the prototype setup are produced by Hamamatsu© model S2387-110R and they have the following characteristics:

Active area diameter	$10\,mm$
Wavelength Range.	$320 \div 1100\,nm$
Photo sensitivity	$0.58\,A/W$ at peak
Dark current Max.	$0.2\,nA$
Terminal capacitance	$1.2 \cdot 10^4\,pF$

In figure 3.5 the power spectral density of signal of the obscured photodiode is shown. As it can be seen, in absence of signal, the photodiode noise, considering also the electronic and the acquisition system noise, is quite constant in frequency and it is about $25\mu V/\sqrt{Hz}$.

3.2 Electronic setup and acquisition system

The signal coming from the photodiodes, from the lockin amplifier and from the episensor are collected by an acquisition system. This is composed by an analog pre-processing board followed by the analog to digital converter (ADC) board. The analog pre-processing consists in amplifying the signals to fit their amplitude to the ADC converters dynamics. In the appendix 4.3, the electronic schemes of the amplifiers for photodiodes and for the episensor signals respectively are shown. All the chain is shown in figure 3.6.

Then the signals are filtered with suitable anti-aliasing filters. In our experiment we use a 16 bit ADCs, so we have a dynamic range of $96\,dB$. The implemented antialiasing filter guarantees that, for sampling frequency above the frequency of about $470\,Hz$, we have a aliasing error lower of ADC noise. The filter is an eight order Chebyschev low pass filter with a band pass ripple of $0.5dB$ and a cut-off frequency of $200Hz$. Each filter used in the acquisition system was characterized
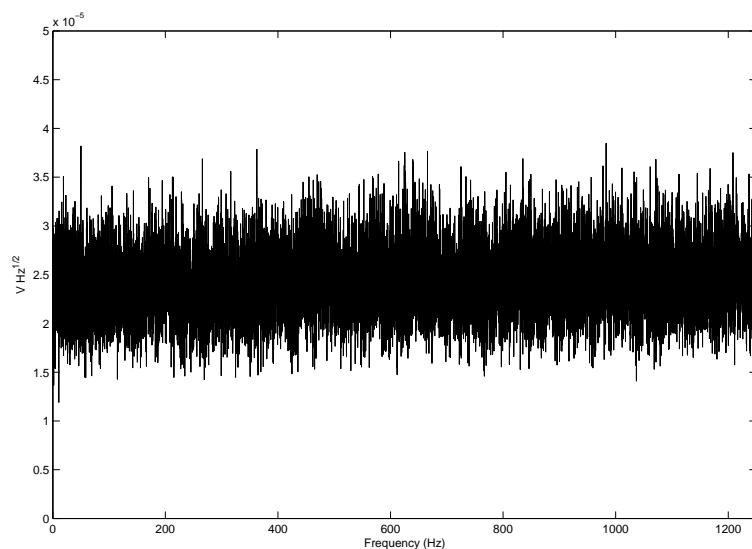
Figure 3.5: Photodiode noise.

63
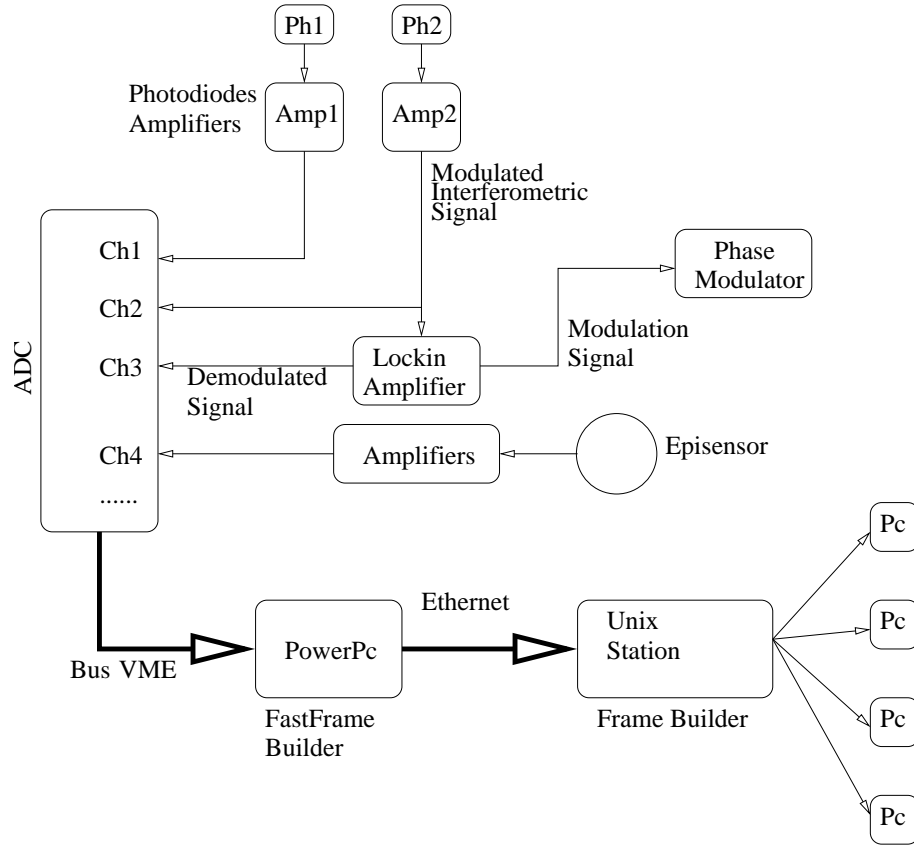
Figure 3.6: Data Acquisition system.

to ensure that its behavior coincides with the one used in the calculated response. In appendix the electronic scheme of antialiasing filter is shown and its magnitude response is shown in figure 3.7.

The digital converter consists of a VME board equipped with a 16 bit ADC with 32 channels. The sampling frequency Fs is fixed at $5000\,Hz$ for the tests, in order to guarantee very good performances of the antialiasing filters. Consider the equation 2.53, in this configuration the instrument is able to measure a maximum acceleration of

$$a_p < \frac{\lambda v_m Fs}{4nL} \approx 3.15\,\frac{m}{s^2} \tag{3.4}$$

for $v_m \approx 800 m/s$, as calculated in the next paragraph. The ADCs noise measured
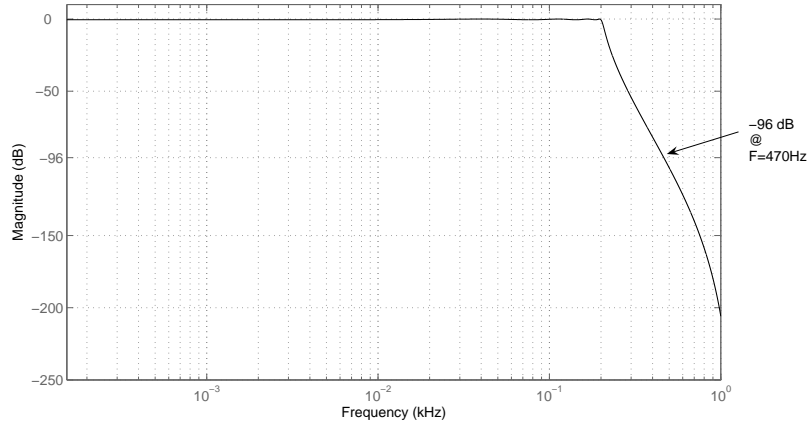
Figure 3.7: Frequency response of the antialiasing filter.

by two channels is shown in figure 3.8. As can be seen, it is constant in band it is
$\sim 1.5\,\mu V/\sqrt{Hz}$.

Actually the phase shift induced by the filtering is not significant for the following analysis, because all signals are affected by the same shift. The sampling frequency is generated by an internal clock of the ADC board and the general timing system is simply the CPU clock. This arrangement is very useful during the test phase, but for setting up a complete measurement system a GPS timing board is necessary to provide a precise timing to perform coincidence with other seismic stations.

The ADC board is managed by a PowerPC CPU based computer board on VME bus, running LynxOS operating system. The CPU collects the data acquired by the ADC and pack them in frames, each one 1 second long. These frames are then sent to a workstation for the analysis through a Fast Ethernet network. The frames are then packed together in longer frames and analyzed. The analysis process does not require high computing power and therefore is performed in real-time. The processed data are packed again and sent to another workstation, equipped with a very large hard disk space, for the final storage.

65
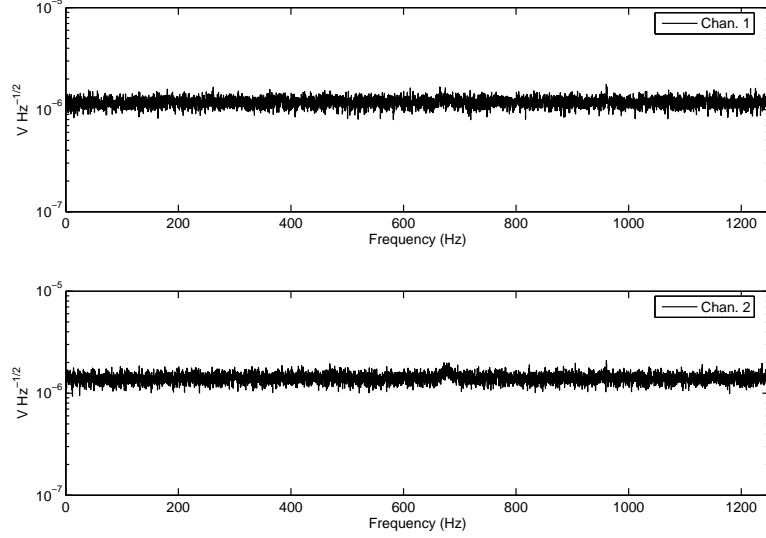
Figure 3.8: Measured ADCs noise for two channels.

3.3 Experimental results

In the following we present the experimental results of implemented prototype. Consider the figure 3.1, using the signal coming from the photodiode 1 $(Ph_1(t))$, it is possible to reduce the fluctuations of interference signal $(Ph_2(t))$. In fact, if there is a variation $\Delta I(t)$ in the laser power $I(t)$, the photodiode 1 measures the quantity

$$Ph_1(t) = k(I(t) + \Delta I(t)) \tag{3.5}$$

where k is the fraction of the laser beam separated by the beam splitter (in theory k is 0.5). The photodiode 2 measures the quantity

$$Ph_2(t) = \frac{(1-k)(I(t) + \Delta I(t))}{2}[1 + C\cos(\phi(t))] \tag{3.6}$$

where C is the visibility of the fringes. If we consider the ratio

$$\frac{Ph_2(t)}{Ph_1(t)} = \frac{(1-k)}{2k}[1 + C\cos(\phi(t))] \tag{3.7}$$

66

it is possible to eliminate the laser power fluctuations $\Delta I(t)$.

At this point it is necessary to understand the signal to noise ratio (SNR) of the instrument. Defining the signal to noise ration as

$$\mathrm{SNR} = \frac{\int |S(f)|^2 df}{\int |N(f)|^2 df} \tag{3.8}$$

in figure 3.9 the power spectral density of the acquisition system noise, measured with laser off, and of the interferometer signal are shown. In our experimental arrangement the SNR results about $20\,dB$ in the band $[0.1 \div 100]\,Hz$.
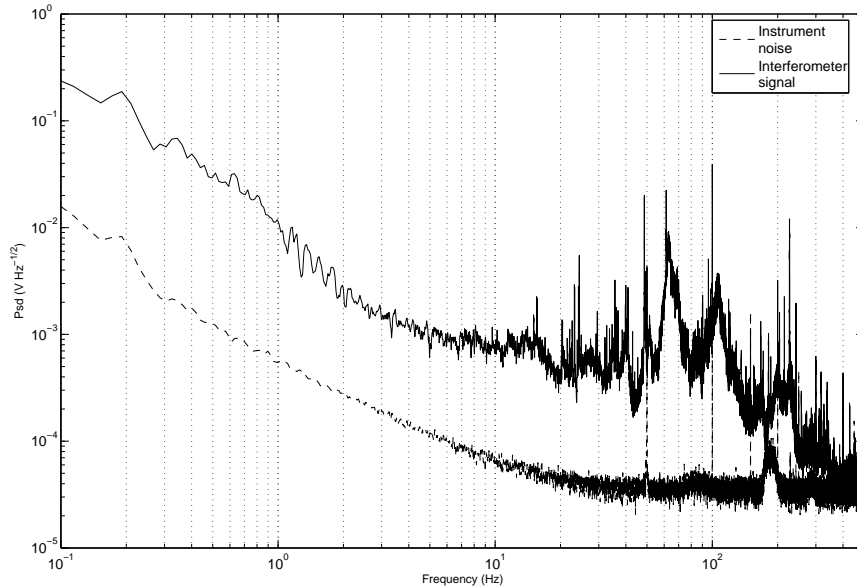
Figure 3.9: Instrument SNR.

As illustrated in the section 2.3.1, the first step of the procedure is the quadrature correction to normalize the interferometer signal and the lockin signal in the range $[-1 : 1]$. In figure 3.10 the parametric plot of the interferometer and of the lockin signal is shown. As it can be seen, after the quadrature correction, the Lissajous figure is corrected and the data are arranged on a circle.

After the phase correction, the phase unwrapping algorithm is applied to recover the interferometer phase without ambiguity using the equation 2.57. Afterward, it
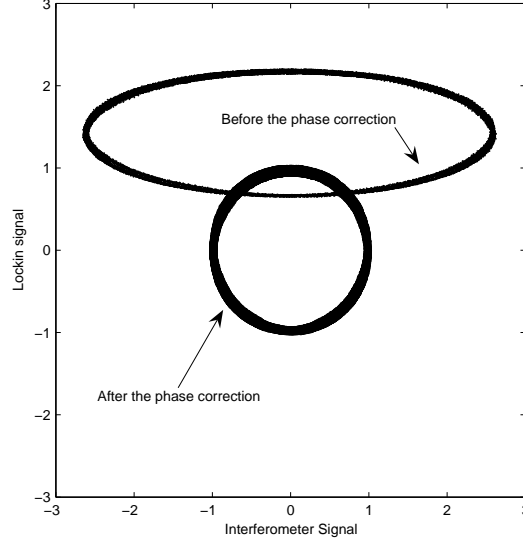
Figure 3.10: A phase correction algorithm example is shown. As can be seen, after the algorithm runs, the Liseau figure is a circle.

is necessary to use the equation 2.36 to calculate the ground acceleration. The numerical derivative of the phase is calculated using the central differences algorithms (see appendix 4.3) approximating the derivative as

$$\frac{d\phi(t)}{dt} \approx \frac{\phi(n+1) - \phi(n-1)}{2\Delta t} \tag{3.9}$$

In figure 3.11 the power spectral density of acceleration measured by the episensor and by the interferometer. It easy to verify the good agreement between the two instruments in the the band $1\pm50\,Hz$. The empirical value t_0 is evaluated comparing the power spectral density of the acceleration measured by the episensor and by the interferometer, shown. Considering the interferometer arm-length, the velocity on the ground of the acoustic waves in our laboratory is about $800\,m/s$.

Since the prototype is not in vacuum, it is important to evaluate the influence of the air pressure fluctuation. For this reason two microphones are used to measure the influence of the fluctuations of air pressure in the interferometer output. In
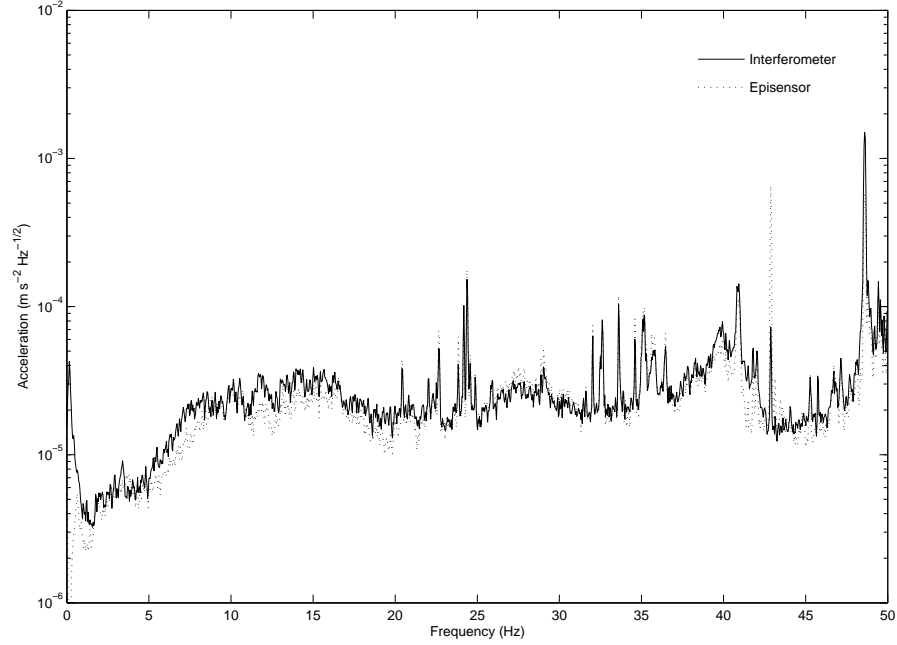
Figure 3.11: Power Spectral Density of acceleration measured by the episensor (dots) and by the interferometer (line).

figure 3.12 the power spectral density of acceleration measured by the episensor (dots) and by the interferometer (line), compared with the microphone's signal and, as can be seen, there are several common frequency resonances.

To understand the influence of the air pressure fluctuations in the interferometer and the episensor measure, also the coherence function is calculated. The coherence between two signals, $f(t)$ and $g(t)$, is defined as

$$C(f) = \frac{\int f(t)g(t)e^{-i2\pi ft}dt}{\left(\int f(t)e^{-i2\pi ft}dt\right)\left(\int g(t)e^{-i2\pi ft}dt\right)} \tag{3.10}$$

The function $C(f)$ varies in the range $[0,1]$ and it measures the correlation degree at the frequency f. The coherence function between the interferometer the microphones output and between the episensor the microphones outputs are shown in figure 3.13. As it can be seen, the effects of the fans of the air conditioner are relevant in the band
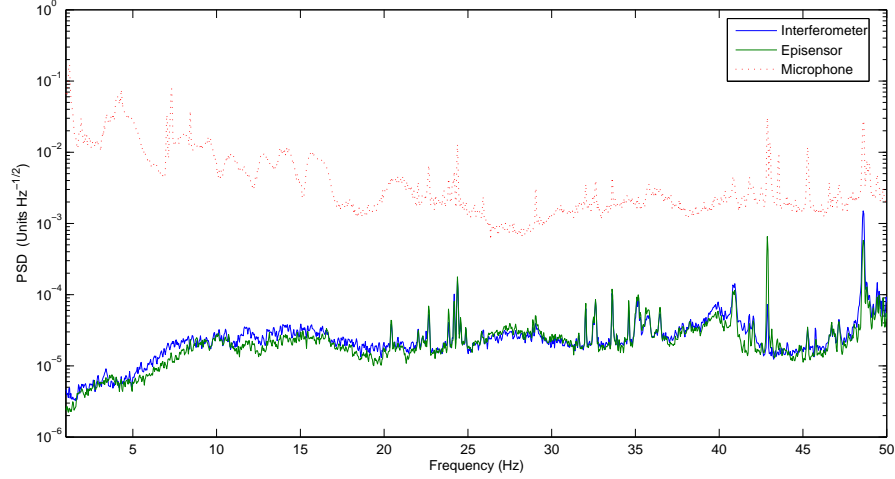
Figure 3.12: Power Spectral Density of acceleration measured by the episensor (dots) and by the interferometer (line), compared with the microphone's signal.

$20 \div 40\,Hz$, while in the band $40 \div 200\,Hz$ also the resonances of the air pressure, related to the room dimension are present. In fact, considering the linear dimension of laboratory L_i where the instrument is installed, it is possible to calculate these resonances using the equation $f_n = n\frac{v}{2L_i}$, where v is the sound wave velocity. For example, the first two harmonics of the air pressure resonance in the laboratory at the temperature of $27° C$ are shown in the table 3.2. The equation we use to evaluate the sound velocity is

$$v = \sqrt{\frac{7}{5}\left(\frac{RT}{0.029}\right)} \tag{3.11}$$

where R is the gas constant and T is the temperature in Kelvin.

To reduce the influence of the acoustic noise, the interferometer has been protected with a cover. Of course, monitoring the pressure and the temperature of the air, the environmental effects can be controlled and reduced. In figure 3.14 the power spectral density of the acceleration measured by the episensor and by the interferometer in the new configuration is shown. As can be seen, reducing the air
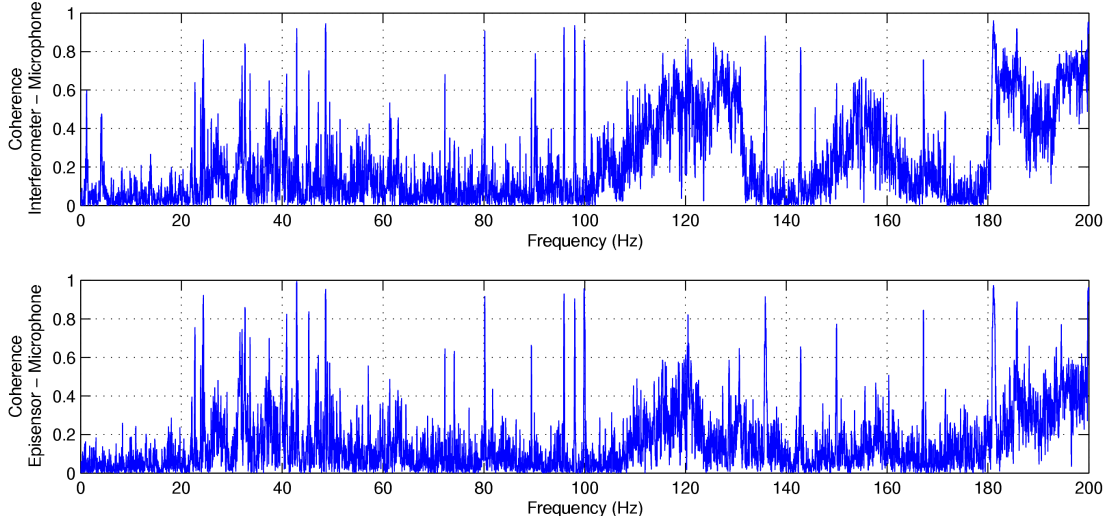
Figure 3.13: Coherence function between the microphones and the interferometer (top) and between the microphone and the episensor (bottom).

	x	y	z
Dimension (m)	4.5	8.7	2.5
First resonances (Hz)	77	40	139
Second resonances (Hz)	154	80	278

Table 3.2: Resonances of the air pressure in the laboratory.

pressure fluctuations the accordance is better in the frequency band until $100\,Hz$. The signal at frequency $\approx 17\,Hz$ must be yet understood. The decreasing of the sensitivity in the low frequency band is probably due to the laser frequency noise and to the fluctuations of the index of the refraction. We have to consider also that in the case of low frequency wave, the wave velocity can be so high that the sampling frequency is not enough high to measure the fringe frequency (see figure 2.7), and this reduces the sensitivity at low frequency,

In figure 3.15 the time evolution of the acceleration measured by the episensor and by the interferometer is shown. As it can be seen, the sensitivity of the interfer-
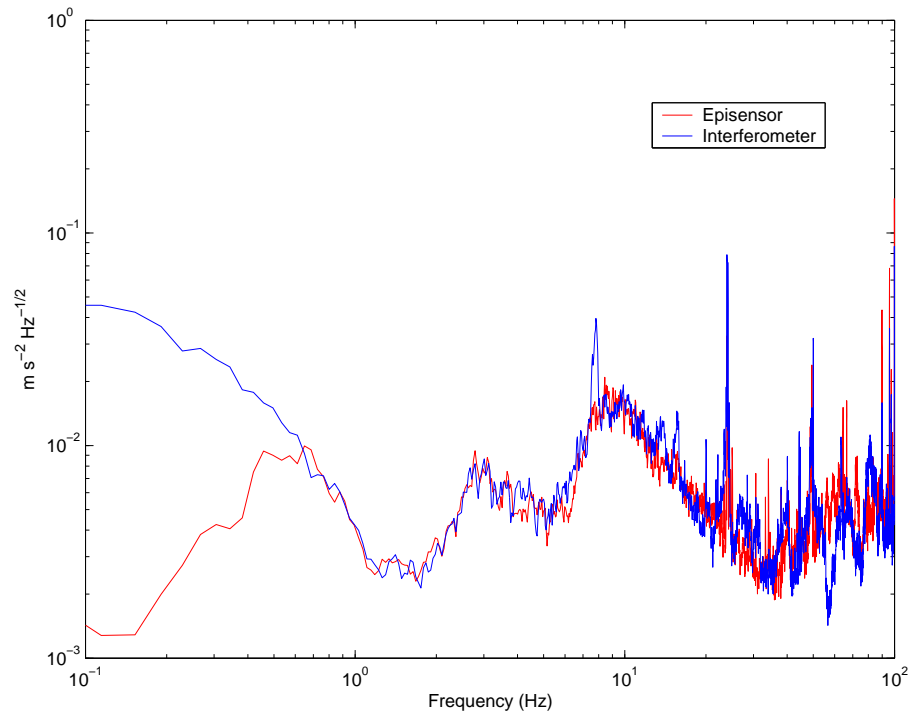
Figure 3.14: Psd of the acceleration measured by the episensor and by the protected interferometer.

ometer is enough to reveal a particular structure in the data: in fact the acceleration measured by the interferometer seems composed by separable different signals. A more accurate analysis it is necessary to understand the sources of these signals. Note that these signals are not clearly present in the episensor output, probably due to the high noise level at high frequency.
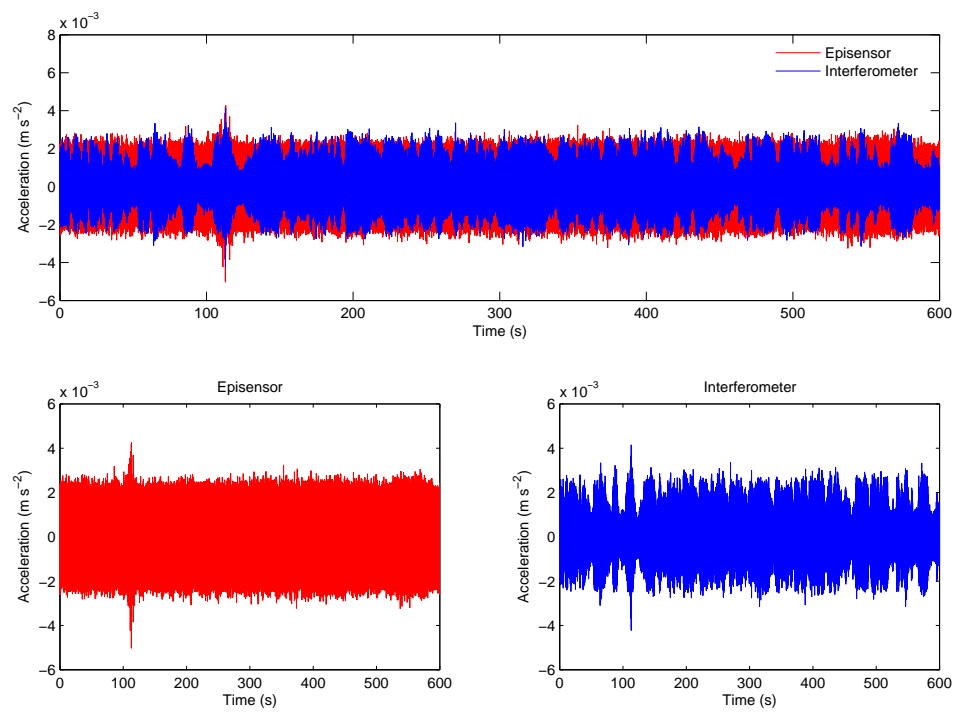
Figure 3.15: Time evolution of acceleration measured by the episensor and by the interferometer.

Chapter 4

Suspended Interferometric prototype

In the previous chapter we have discussed as a laser strainmeter can be used as a velocimenter for seismic waves measurement. We have made several approximations and we have revealed the following problems:

- The sensitivity in the frequency band $f < 0.5\,Hz$ is too low and so it has been improved;

- the instrument noise is still too much high; the sensitivity can be improved

  - developing an automatic alignment procedure to reduce the noise induced by the non perfect and non stabilized alignment of the recombined laser beams on the photodiode;

  - sheltering the instrument by air pressure and temperature fluctuations;

  - using a laser source stabilized in frequency;

- in the case of earthquake, the displacement can be enough large to misalignment the laser beams and so it is necessary to improve the linearity of the

instrument.

For this reason we have projected a highly sensitive wide-band seismometer which can detect the horizontal component of the ground acceleration, and a simple test system has been realized.

4.1 Principle

We made use of a pendulum as a reference of vibration detection. Suppose that a pendulum, whose resonant frequency is $f_0 = \omega_0/2\pi$ and whose quality factor is Q, is suspended with an external force of f_e, applied to mass m. We can describe this system with the following equation of motion:

$$\ddot{x} + \frac{\omega_0}{Q}(\dot{x} - \dot{y}) + \omega_0^2(x - y) = \frac{f_e}{m} \tag{4.1}$$

where x and y denote the displacement of the pendulum mass and that of the suspension point, respectively.

By introducing a relative displacement $d = x - y$ and the Fourier transform, equation 4.1 becomes

$$d(\omega) = \left(-\omega^2 y(\omega) - \frac{f_e(\omega)}{m}\right) H(\omega) \tag{4.2}$$

where the transfer function of the pendulum $H(\omega)$ is

$$H(\omega) = \frac{1}{-\omega^2 + i(\omega_0/Q)\omega + \omega_0^2} \tag{4.3}$$

If we control the force f_e so as to make d constant using a feedback filter with a transfer function $F(\omega)$, from the feedback force we can obtain the vibration spectrum of the ground as

$$|y(\omega)| = \frac{|f_e(\omega)|}{m} \frac{1}{\omega^2} \left|\frac{1 + H(\omega)F(\omega)}{H(\omega)F(\omega)}\right| \tag{4.4}$$

If we prepare a feedback filter that satisfies $|H(\omega)F(\omega)| \gg 1$ over a wide frequency range and read-in a feedback signal, we can create a wideband seismometer: in fact $f_e(\omega)/m = \omega^2 y(\omega)$ directly express the acceleration of the ground. If the condition $H(\omega)F(\omega) \gg 1$ is not satisfied, we use the closed loop transfer function to measure the ground acceleration as

$$|a_y(\omega)| = \omega^2 y(\omega) \left(\frac{1 + H(\omega)F(\omega)}{H(\omega)F(\omega)} \right) \frac{f_e(\omega)}{m} \tag{4.5}$$

Schematic figure 4.1 shows a pendulum and the laser, beam splitter, as well as the fixed and the free mirror that form the Michelson interferometer. Assuming that the fixed mirror moves together with the ground, we can detect the relative displacement d between the ground and the pendulum mass, from the fringe signal detected by the photodiode. An interferometer allows a highly sensitive detection of the displacement thus leading to a very sensitive seismometers. This fringe signal is analyzed to recover the pendulum displacement and this signal is feed back through the feedback filter as forces to the pendulum on which the free mirror is attached. The feedback force f_e is applied as a magnetic interaction between the magnets on the pendulum and the magnetic field produced by the coils. Because the current of the coil is proportional to f_e, we can obtain the horizontal component, in the "free mirror"-"beam splitter" direction, of the acceleration of the ground from the current using equation 4.4.

4.2   Developed prototype

The seismometer which we actually have made differs slightly from that shown in figure 4.1 and it is implemented mainly to test the possibility to realize of a different kind, and we hope, more accurate instrument. All the components are mounted on a optical table within an episensor to verify the results. The experimental setup is composed by a Michelson interferometer, like that shown in figure 3.1, where
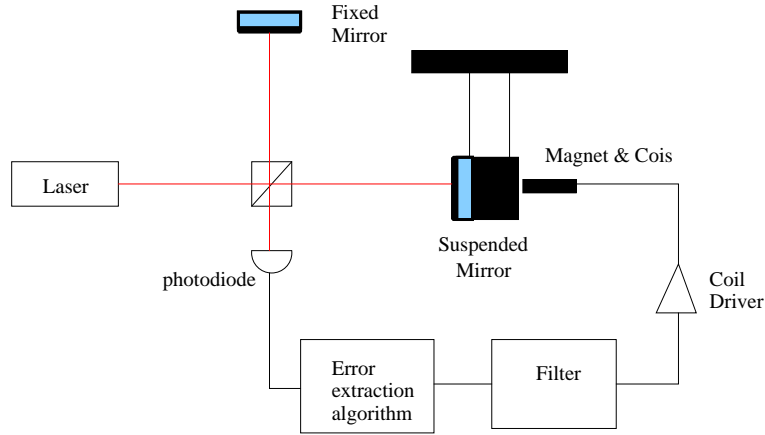
Figure 4.1: Block diagram of the feedback system.

the free mirror is fixed on a double pendulum, shown in figure 4.2, as suspended system. The interferometer armlengths are about $40\,cm$ long. The double pendulum is chosen because, it is equivalent to a low pass mechanical filter with good isolation above the frequency corner with an amplitude attenuation $propto(f/f_0)^4$, where f_0 is the resonant frequency. This configuration corresponds to have an attenuation of $80\,dB/dec$ above f_0. In this way the suspended mass can be consider "free" and it can be used as a inertial mass. More complex techniques to reduce the resonant frequency and to increase the attenuation factor above the resonant frequency are section 4.3.

The double pendulum is composed by two masses:

- the upper mass is an aluminum parallelepiped of dimension $14 \times 14 \times 12\,cm$ and mass $6.5, Kg$, suspended in the barycenter to the tower with a steel wire $12\,cm$ long and $0.2\,mm$ width. On the side of this mass there are four magnets used, together with coils mounted on the tower, to force the mass position.

- the bottom mass is a cylindrical mass of $3.2\,Kg$ suspended to upper mass using two aluminum wire. On the front side of this mass a mirror is fixed.

All the wires are fixed using special supports to reduce the energy loss due to the
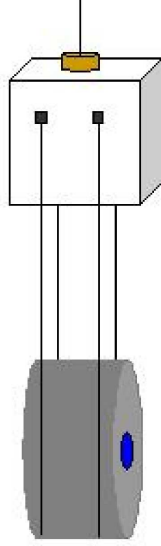
Figure 4.2: Pictures of the double pendulum.

friction.

4.2.1 The reading system

To control the upper mass of the double pendulum, we implement a position reading system based on optical lever and bidimensional photodiodes, called position sensing detector (psd). The optical scheme of a psd is shown in figure 4.3.

We use the psd model S2044 produced by Hamamatzu©. The sensitive surface is a square with concave sides to reduce the non linear effects of the borders and with four electrodes. The spatial resolution of this sensor is about $0.6 \, \mu m$. The current signal of each electrodes is converted in a voltage signal by an amplifier. To obtain a signal proportional to the coordinates of the laser beam in a reference system centered in the photodiode, we combine the voltage signal $a : i$ of each electrodes as:

$$x = \frac{a_2 + a_3 - a_1 - a_4}{a_1 + a_2 + a_3 + a_4}$$
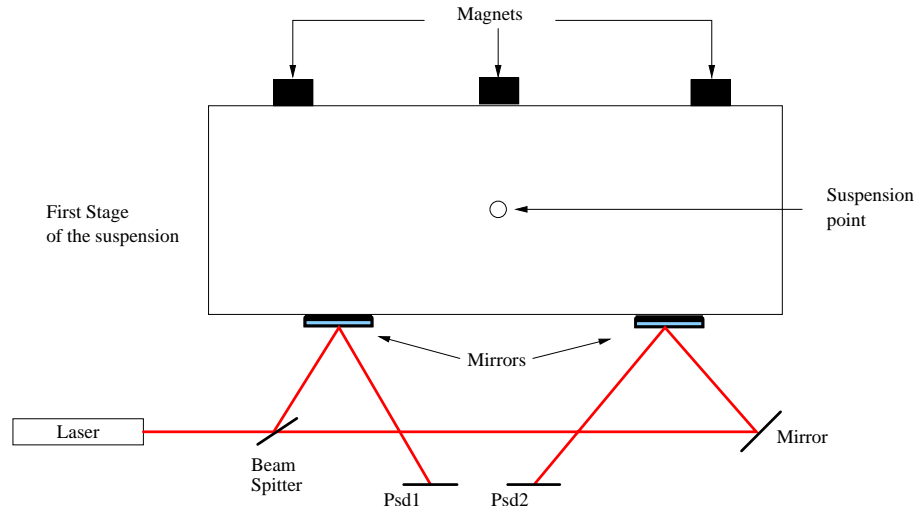
Figure 4.3: Optical Scheme of the reading system.

$$y \quad = \frac{a_1 + a_2 - a_3 - a_4}{a_1 + a_2 + a_3 + a_4} \tag{4.6}$$

In this way it is possible to reconstruct the position of the laser beam on the photodiode surface. In figure 4.4 the scheme of the psd is shown.
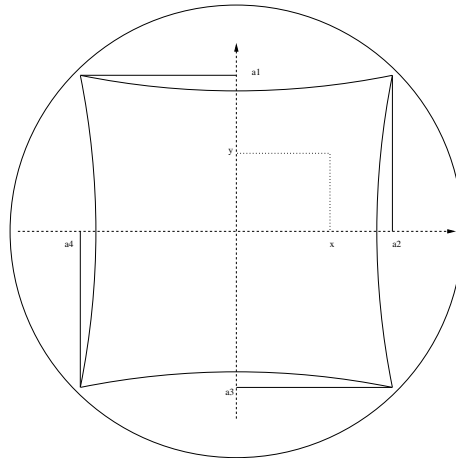
Figure 4.4: Scheme of the position sensitive detector.

The reading system is based on the principle of the optical lever: a laser beam is reflected by the mirror on the mass and it impinges, in ideal condition of fixed mass,

the center of the psd. If there is a movement of the mass, and so of the mirror, there is a movement of the laser beam that we can measure with the psd. It is possible to demonstrate that if we use a single optical lever, we are not able to discriminate between translations and rotations of the mass and. For this reason, we decide to use a double optical lever, composed by two lever with the same geometrical characteristics. This arrangement permits us to measure and translation and rotation of the mass. In fact

- in ideal condition, if the mass moves of a quantity x, the laser beam moves of a quantity

$$\Delta_{t_1} = 2x \tan(i) \tag{4.7}$$

on the first psd and

$$\Delta_{t_2} = -\Delta_{t_1} = -2x \tan(i) \tag{4.8}$$

on the second psd, where i is the impact angle of the laser beam on the mirror, as can be seen in figure 4.5.
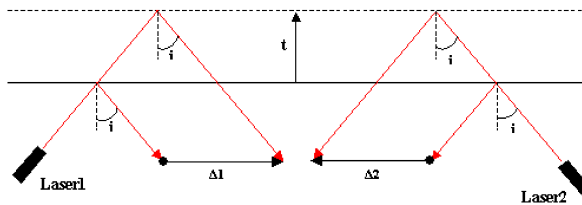
Figure 4.5: Laser beam response to a translation of the mirror.

- in ideal condition, if the mass rotates of an angle δ, the laser beams move in the same sense on each psd of a quantity

$$\Delta_{r_1} = \Delta_{r_2} = \frac{1}{\cos(2\delta + i)} \left[\frac{b \sin(2\delta)}{\cos(i)} - 2L \sin \delta \sin(\delta + i) \right] \tag{4.9}$$

where $2L$ is the distance between the two psd.

80

As can be seen the psd signals contain information both about the translation and about the rotation of the mass. Consider the linear combination

$$\Delta_1 \equiv \Delta_{t_1} + \Delta_{r_1} = \Delta_t + \Delta_r$$
$$\Delta_2 \equiv \Delta_{t_2} + \Delta_{r_2} = -\Delta_t + \Delta_r \quad (4.10)$$

if we defined the function

$$\Delta^+ \equiv \frac{\Delta_{t_1} + \Delta_{r_1}}{2} = \Delta_r$$
$$\Delta^- \equiv \frac{\Delta_{t_2} + \Delta_{r_2}}{2} = -\Delta_t \quad (4.11)$$

we obtain a signal Δ^+ proportional only to the rotation and a signal Δ^- proportional only to the translation. In this way we have uncoupled the two movements and we are able to use these signals as error signals for the control filters.

If there is an asymmetric of the reading system, we have to replace the equations 4.11 with

$$\Delta^+ \equiv a_1 \Delta_{t_1} + b_1 \Delta_{r_1}$$
$$\Delta^- \equiv a_2 \Delta_{t_2} + b_2 \Delta_{r_2} \quad (4.12)$$

where the coefficients have to be calculated using a statistical fit on experimental data. Of course, to read all six degrees of freedom, we have to place a double optical lever on each side of the mass.
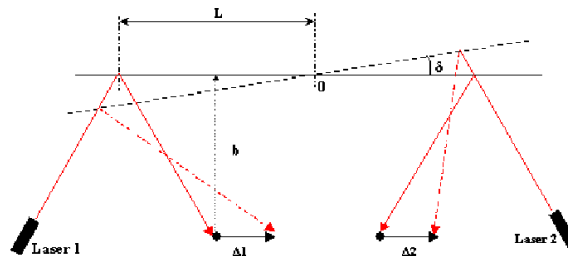
Figure 4.6: Laser beam response to a rotation of the mirror.

4.2.2 The digital control system

The feedback system used in the experimental setup is composed by

- the reading system, based on a double optical lever implemented using a single laser source, a beam splitter and three mirror and two photodiodes;

- the conditioner amplifiers, used to convert the current signals of the photodiodes in voltage signals, amplified to match the ADC dynamics;

- the 16 bit ADC, which converts the voltage signals in digital signals;

- the CPU, which reads the digital data from the ADC, converts these signals in mass position using the equation 4.12, calculates the control signal and it send this signal to the DAC;

- the 16 bit DAC, which converts the digital control signals into analog signals and send them to the coils' driver.

- the actuation system, which is composed by four coil fixed on the mechanical support, aligned to four magnets fixed on the oscillating mass. With this arrangement we are able to apply and longitudinal force and torsional momentum.

The complete scheme of the control system is shown in figure 4.7, where are visible only two magnets and two coils instead four for simplicity.

Consider the reference system on the upper mass shown in figure 4.8, it is possible to obtain the error signal using the equation

$$
\begin{aligned}
\theta_y &\propto \Delta x_1 + \Delta x_2 \\
z &\propto \Delta x_1 - \Delta x_2 \\
\theta_x &\propto \Delta y_1 + \Delta y_2
\end{aligned}
\tag{4.13}
$$
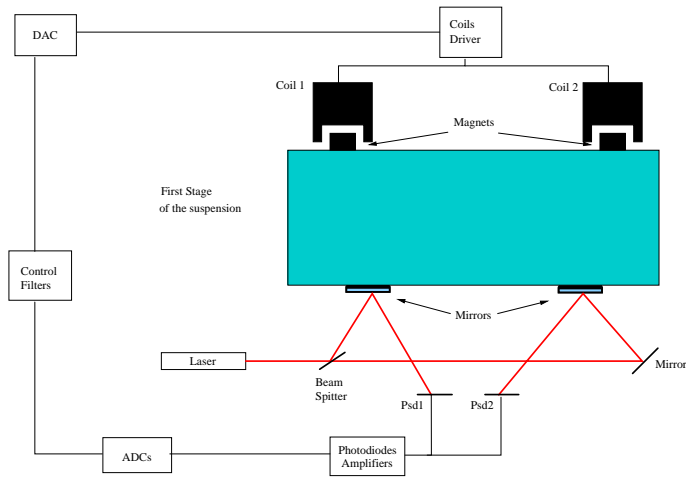
Figure 4.7: Control system scheme.

where $Deltax_1$, Δx_2, Δy_1 and Δy_2 are the position of the laser beams on the two psd.
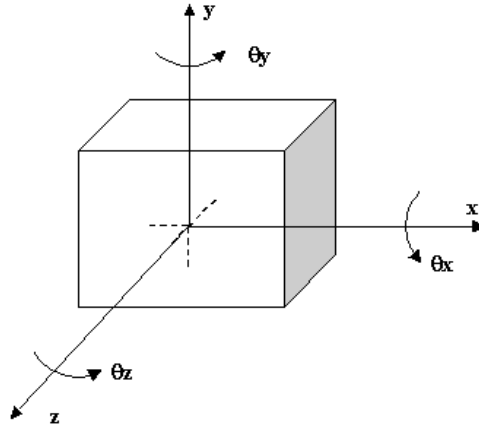
Figure 4.8: Reference system on the upper mass.

The theoretical model of the suspension

Unfortunately we are not able to measure the open loop transfer function of the suspended masses because the motion is too large that the laser beams go out the

sensitive surface of the position sensing photodiodes. To overcome this problem we choose to analyze the suspended system by the theoretical point of view. For this task we calculate the Lagrange equations for the six degree of freedom of masses. In the approximation of small displacement we linearize the Lagrange equation and we calculate the transfer functions that link the motion of the suspended point with the variables x, y, z, θ_x, θ_y and θ_z fro each mass and so we estimate the frequencies of the normal modes. Just as an example, considering the upper mass, for the tilt mode θ_y and θ_x we calculate the following transfer functions:

$$
\begin{aligned}
H_{\theta_x}(s) &= 1150 \frac{(s^2 + 0.002s + 405.8)}{(s^2 + 0.002s + 6.645)(s^2 + 0.002s + 522.4)} \\
H_{\theta_y}(s) &= 4.685 \frac{(s^2 + 0.002s + 94.94)}{(s^2 + 0.002s + 0.0363)(s^2 + 0.002s + 118.2)}
\end{aligned}
\tag{4.14}
$$

where the dc gain is determined using the measured transfer function in closed loop. In figure 4.9 the transfer function of the rotational degrees of freedom of the upper mass, θ_x, θ_y, is shown. As it can be seen there are two resonant frequency ($0.41\,Hz$ and $3.64\,Hz$ for θ_x and $0.03\,Hz$ and $1.73\,Hz$ for θ_y) and a zero factor due to the bottom mass for each degree of freedom.

In figure 4.10 the transfer function of lower mass, for the z degrees of freedom is shown. As it can be seen there are two resonant frequencies ($0.78\,Hz$ and $1.56\,Hz$). Because the z-axis is one of the two optical axis of Michelson interferometer, this degree of freedom has to be controlled used the error signal extracted from the interferometer signal. This is the sensitive part of the instrument.

The control filters

Calculated the theoretical transfer functions, we use them to implement the control filters for the tilt mode of the upper mass. In this way the longitudinal mode of the lower mass, that is measured by the interferometer, is, at the moment, the only not controlled mode. The control filters for θ_x and θ_y are shown in figure 4.11 and they
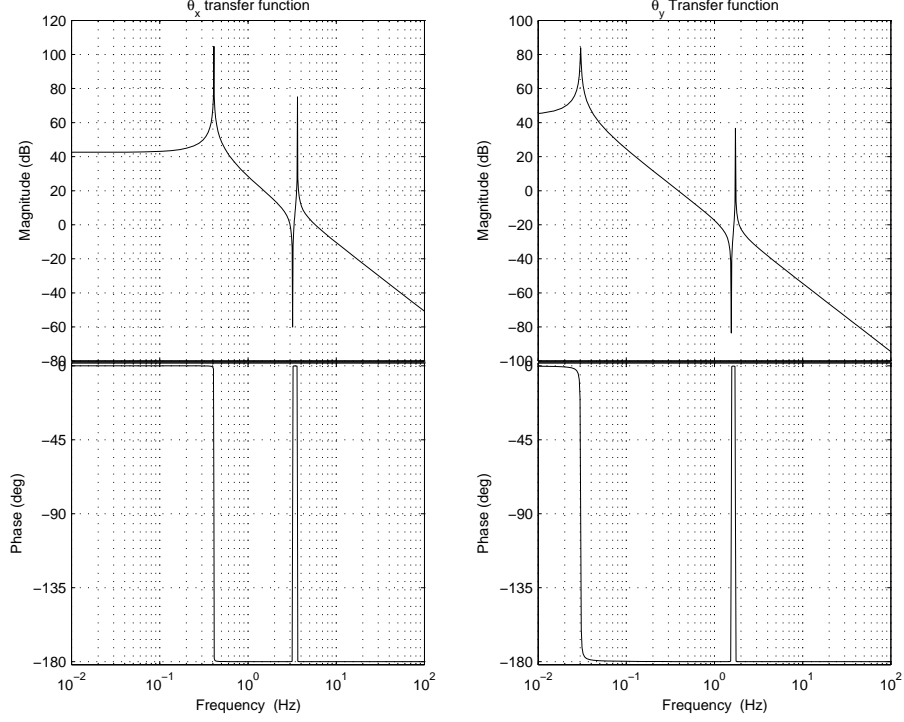
Figure 4.9: Transfer functions for the rotational degrees of freedom of the upper mass.

are described by the following equations:

$$
\begin{aligned}
G_{\theta_x} &= K_1 \frac{1}{s}\left(s^2 + \frac{2\pi 0.13}{0.5}s + (2\pi 0.13)^2\right)\left(\frac{s^2 + \frac{2\pi 0.67}{100}s + (2\pi 0.67)^2}{s^2 + \frac{2\pi 0.67}{2.5}s + (2\pi 0.67)^2}\right) \times \\
&\quad \times \left(\frac{s^2 + \frac{2\pi 1.4}{10}s + (2\pi 1.4)^2}{s^2 + \frac{2\pi 1.4}{2}s + (2\pi 1.4)^2}\right)\left(\frac{1}{s^2 + \frac{2\pi 17.3}{0.5}s + (2\pi 17.3)^2}\right) \qquad (4.15)\\
G_{\theta_y} &= K_2 \frac{1}{s}\left(s^2 + \frac{2\pi 0.364}{0.5}s + (2\pi 0.364)^2\right)\left(\frac{s^2 + \frac{2\pi 1.165}{100}s + (2\pi 1.165)^2}{s^2 + \frac{2\pi 1.165}{2.5}s + (2\pi 1.165)^2}\right) \times \\
&\quad \times \left(\frac{1}{s^2 + \frac{2\pi 36.4}{0.5}s + (2\pi 36.4)^2}\right) \qquad (4.16)
\end{aligned}
$$

where K_1 and K_2 are the gains of each control filter.

The closed loop transfer functions (for the tilt mode of the upper mass) are shown in figure 4.12.

85
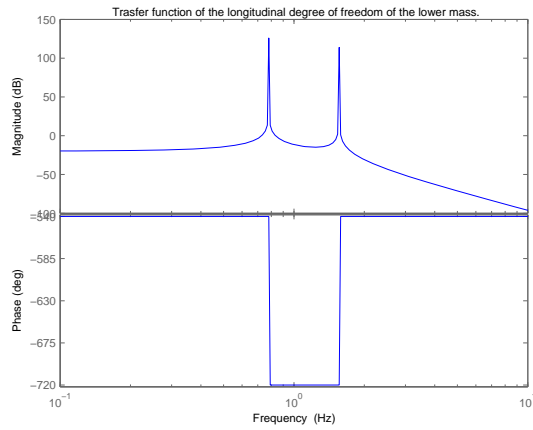
Figure 4.10: Transfer function for the longitudinal (z axis) degrees of freedom of the lower mass.
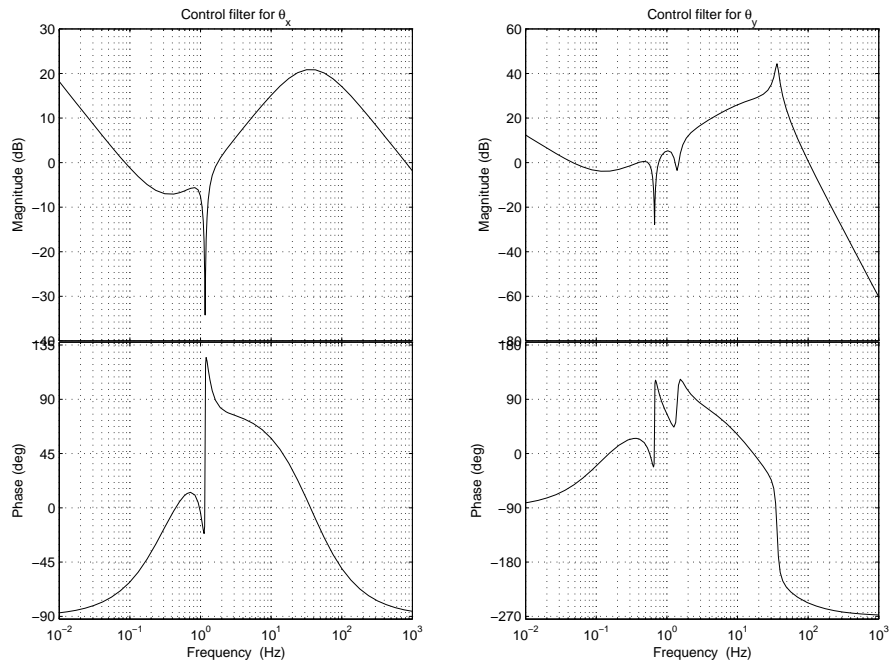
Figure 4.11: Control filter for θ_x and θ_y.

86
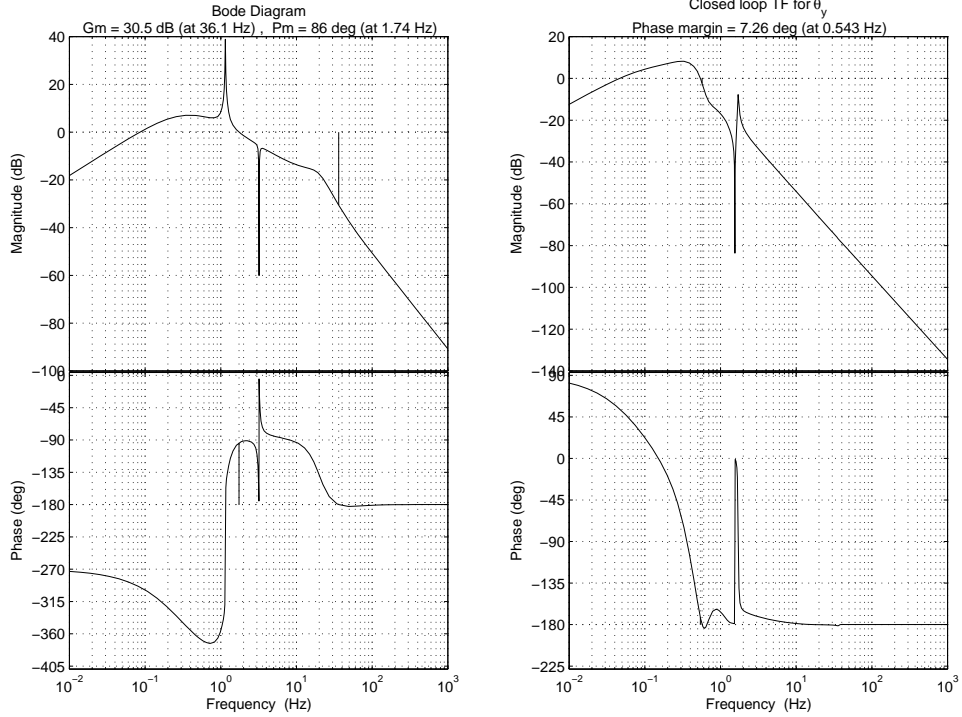
Figure 4.12: Closed loop transfer function for the θ_x and for the θ_y modes.

4.2.3 Experimental results

In this chapter we show only very preliminary results about the force feedback prototype. Consider that the angular degrees of freedom of the upper mass of the suspended system are controlled, there is a residual motion of $\approx 100\mu rad$ for θ_x and $\approx 50\mu rad$ for θ_y, as can be seen in figure 4.13.

In this configuration, the only not controlled motion is the longitudinal mode along the z-axis. The movement of the bottom mass along this axis is measured with the Michelson interferometer and, using the phase-unwrapping algorithm, we can reconstruct the displacement. Now we can follow two principal strategies:

- we use the pendulum as an inertial seismometer with natural frequency of about $3\,Hz$. In this way, for frequencies above of the natural frequency, the
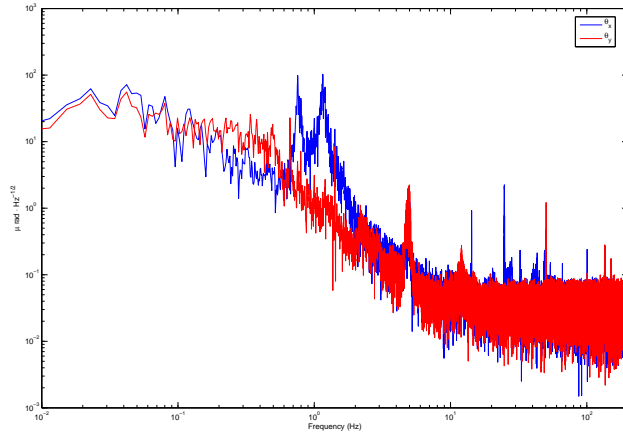
Figure 4.13: Power Spectral Density of the residual angular motion of the upper mass of the suspension.

> bottom mass can be considered "free" and the pendulum is a displacement sensor with the accuracy given by the interferometric readout.

- we use the displacement signal reconstructed analyzing the interferometer signal as error signal to control also the movement along the z-axis. In this way we have realized a force feedback accelerometer with interferometric readout.

Unfortunately, at the moment, we have not possibility to act on the back of the bottom mass, so we are able only to evaluate the response of the system to ground motion using the instrument as an passive seismometer. In this way we also test the interferometric readout system. In figure 4.14 the power spectral density of the signal reconstructed analyzing the interferometer fringes is shown.

As it can be seen the low frequency part ($f \lesssim 0.5\,Hz$) is dominated by the effect of the derivative algorithm[1]. In the band $0.5 \lesssim f \lesssim 3\,Hz$ the characteristic

---

[1]To obtain the acceleration spectrum from measurement of displacement, we have to calculate the second derivative of the data and this corresponds to multiply the displacement spectrum by a factor $(2\pi f)^2$.
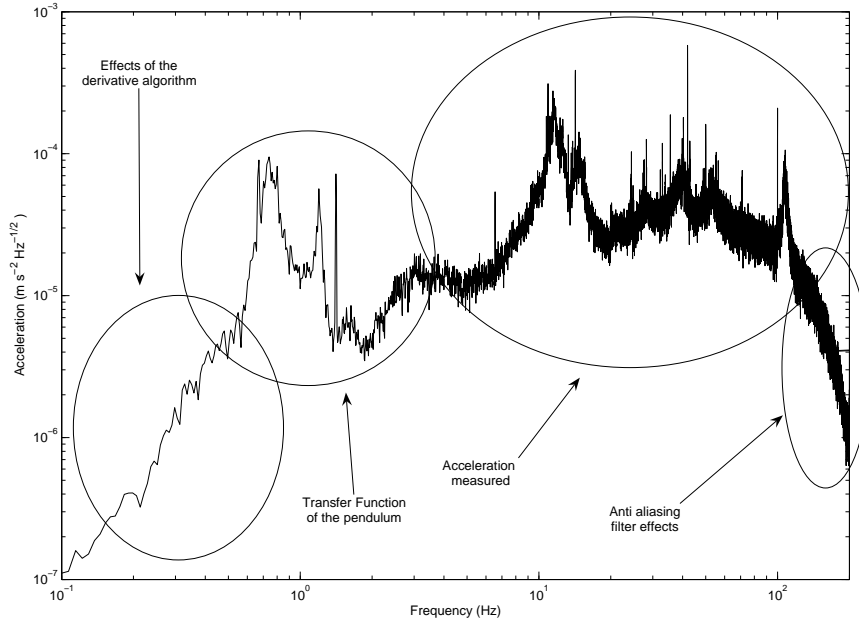
Figure 4.14: Power Spectral Density of the longitudinal mode as measured with the interferometer.

frequency shape of the pendulum transfer function is present. In fact it can be seen the longitudinal motion of the bottom mass, and also several frequency peaks due to the residual angular tilt of the masses coupled between them. In the frequency band $f \gtrsim 3\,Hz$, the control transfer function has not relevant effects on pendulum mode and the low pass mechanical filter realized by the suspension decreases the motion of the bottom mass so that it can be consider "free". In this band the interferometer signal is related directly to the ground motion. For frequency greater of $100\,Hz$, the effect of the antialiasing filters are dominants.

It is interesting also to evaluate the transfer function which links the acceleration of the ground, measured with an episensor, and the acceleration measured by the interferometer, shown in figure 4.15. As it can be seen, at low frequency the interferometer mainly measure the motion of the pendulum. In the band $2 \div 15\,Hz$ the transfer function is approximately 1 and so the interferometric sensor measure

89

correctly the ground motion. At frequency greater than $20\,Hz$, the effect of the air conditioner and the effect of misalignment of the arms of the interferometer are present. As it can be seen there is also an increase of the control noise due to the uncorrected coupled between different degrees of freedom.
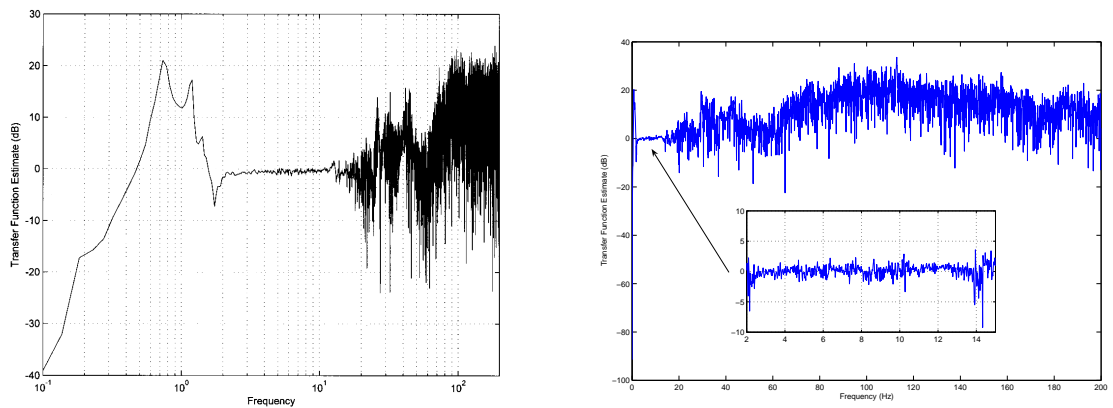

Figure 4.15: Transfer function of the longitudinal mode of the suspended mass.

Of course these are only preliminary results and several improvement must be done, in particular in these direction:

- it is necessary to implement a more robust control filters to reduce some more the angular motion; in fact these movement cause a misleading signal in the interferometer output;

- the effects of the air pressure fluctuations have to be monitor to evaluate their effects to the index of refraction variation and so to the interferometer signal;

- an accurate system of actuators must be design to control also the motion of the bottom mass; this way we can implement a force feedback seismic sensor based on interferometric readout.

- a more compact design have to be developed for testing the sensor in a site.

4.3 Increasing of the measurement band

To increase the frequency band of the interferometric seismometer it is necessary to reduce the frequency corner of the oscillating mechanical part so that it can be consider "free" from ground accelerations with a better approximation.

A particular type of isolator under investigation is an N stage isolation stack consisting of alternating masses and spring. Such a low pass mechanical filter has good isolation above a low-frequency corner with an amplitude attenuation $\approx (f/f_0)^{2N}$, where f_0 is the resonant frequency. Below the corner frequency, N normal modes exist in the response of the stack driven by external disturbances. The amplitudes of these normal modes depend linearly on their Q factor and therefore the resonant mode amplitudes may rise many orders of magnitude higher than the background seismic noise. These peaks need to be attenuated as much as possible.

Various techniques such as magnetic eddy current damping or active damping may be used but a simpler approach would be to use an ultralow frequency (ULF) mechanical low pass filter in a front end, pre-isolation stage. Such a ULF stage could theoretically attenuate the normal mode amplitudes up to six orders of magnitude given a ULF stage with a resonant frequency of $10\,mHz$. Thus a system of isolation stack and ULF stage ($f_0 \approx 10\,mHz$) forms a super attenuator and is theoretically capable of reducing seismic noise by up to a factor of 10^9 on the bottom mass of the suspension.

One approach to creating a ULF filter is by using an inverted pendulum. In this paragraph we investigate the performance and mechanical properties of an inverted pendulum in the form of a horizontal platform capable of onedimensional low-frequency motion. The effect of an inverted pendulum ULF stage on the normal modes of an isolation stack has been modeled and can be seen in figure 4.16. This shows the response of a five-stage isolation stack driven by seismic noise. Curve A shows the response of a five-stage isolation stack alone ($Q = 10^3$); curve B shows

the same stack with a front end ULF stage with a resonant frequency of $10\,mHz$.
The benefits of a ULF stage can be clearly seen with a normal mode attenuation of
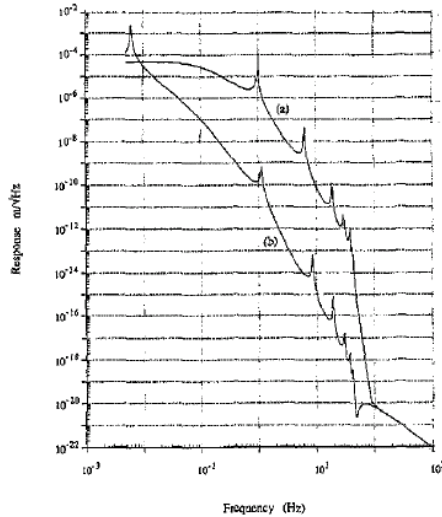up to six orders of magnitude.

Figure 4.16: Theoretical response of a five-stage isolation stack ($Q = 10^3$) supporting
a $1\,m$ pendulum which in turn is supporting the test mass.

To understand the dynamics of an inverted pendulum, a simple ideal mechanical
model can be constructed. An inverted pendulum consists of a platform with given
mass m mounted on top of support rods of length l which act as cantilever springs
and can be displaced by x meters. The restoring spring force (spring constant k),
$F = kx$ acts against the gravitational force (acceleration g) $F_g = -mg\sin(\theta) \approx$
$-(mgx)/l$, assuming the small angle approximation $\sin(\theta) = \theta$. Therefore

$$F = F_g + F_s = \left(k - \frac{mg}{l} \right) x = \hat{k}x \qquad (4.17)$$

and the pendulum undergoes single harmonic motion. Considering the resonant
frequency of a pendulum to be $\omega_0 = 2\pi f_0 = \sqrt{\hat{k}/m}$, the resonant frequency for an
inverted pendulum is given by

$$\omega_0 = \sqrt{\frac{k}{m} - \frac{g}{l}} \qquad (4.18)$$

92

given the condition

$$\frac{k}{m} - \frac{g}{l} \geq 0 \tag{4.19}$$

As can be seen the gravitational component acts as a negative spring which reduces the resonant frequency of the pendulum. However, when the pendulum is damped such that, for a given decay constant η, $k/m \sim \eta^2/4m^2$, then the system has an additional damping term. Therefore the natural frequency can be expressed as

$$\omega_0 = \sqrt{\frac{k}{m} - \left(\frac{g}{l} + \frac{\eta^2}{4m^2}\right)} \tag{4.20}$$

The point at which the resonant frequency is zero is when the gravitational force becomes greater that the restoring force of the spring and the pendulum collapses. This defines the critical mass which is given by

$$m_c = \frac{kl}{g} \tag{4.21}$$

The Q factor of the pendulum can be found by substituting equation 4.18 into the expression for the Q of a generic mechanical system. Thus the Q factor for an inverted pendulum system is given by

$$Q = \sqrt{\frac{klm - gm^2}{l\eta^2}} \tag{4.22}$$

At low frequency the terms in expression 4.18 almost cancel and the pendulum become unstable if the frequency is dependent on the mechanical parameters of the system. With such an instability near the critical mass, it will be necessary to introduce active feedback to control the dynamics of the pendulum which provides an additional negative spring force γ_d to the system [22]. In figure 4.17 the ultra low frequency isolation system is shown. This suspension will be used to develop a suspended Michelson interferometer with Fabry-Perot mode cleaner for seismic noise studies in the VIRGO laboratory, in Naples.
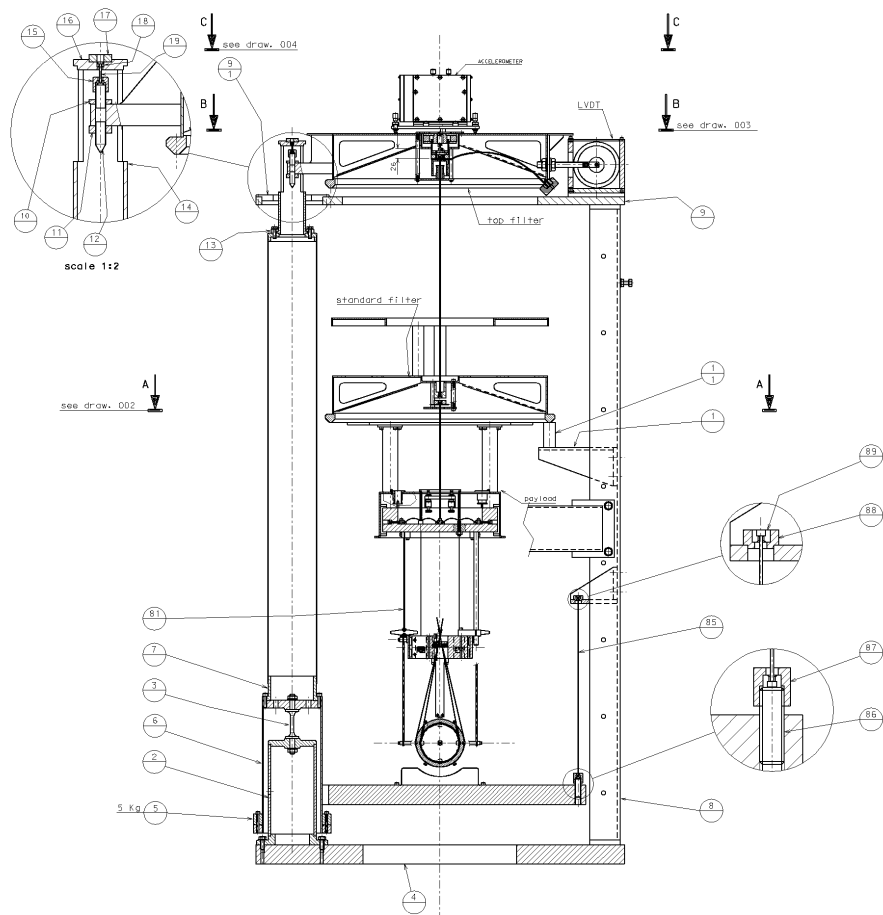
Figure 4.17: Ultra low frequency isolation system developed in the VIRGO laboratory, in Naples.

Conclusions

In this work we have introduce the use of laser beams interferometry for the project of a two new kind of seismic sensors. The main idea was to use the high sensitivity of interferometric technique to measure ground motion.

The first kind of sensor, that we have developed, is shown in chapter 2. This kind of sensor is based on a Michelson interferometer, with a one mirror fixed on the ground and the other one fixed on an bench with the remain optical components. We have demonstrated that the interferometer output is proportional to the velocity of seismic waves. To do this we have:

- calculated the theoretical transfer function in the approximation of seismic wavelength much smaller that interferometer armlengths, calculating the error of this approximation;

- calculated the effects of misalignment on the output of the interferometer in the approximation of plane wavefront;

- evaluated the effects of index of refraction fluctuations;

- calculated the directional sensitivity diagram;

- calculated the conditions for optical matching between the laser beam spot size and the photodiode size;

- optimized the choice of the sampling frequency;

- used an phase-unwrapping algorithms to reconstruct correctly the phase of the laser beam impinging on the output photodiode;

In the chapter 3 the experimental results on a prototype developed to confirm the theoretical results obtained in the chapter 2 is shown. Analyzing the figure 3.14 we can conclude that a preliminary experimental test on this technique confirms the theoretical results, allowing for an interferometric measurements of the ground acceleration that is in good agreement with the measure provided by a standard accelerometer for seismic applications, at least in the frequency band $0.5 \div 100Hz$. The sensitivity of such device should be limited only by the environmental parameters like temperature and pressure, whereas the laser intensity can be continuously monitored in order to take into account its variations. Of course the set-up used was not optimized, and future work is needed in order to obtain further improvements in the signal extraction quality as well as in the noise level of the instrumentation. However the first experimental results are very promising.

In the chapter 4 a suspended prototype is shown. A novel approach, based on optical levers, for reading of the oscillating mass is introduced. With this arrangement we are able to calculating the error signals needed to control the suspended mass. Also in this prototype the reading is made using a Michelson interferometer to archive a high sensitivity. Some preliminary results on the control of the angular motion of the suspension is shown. We can conclude that if we use this prototype as an inertial seismometer, at the frequency above the resonant frequency of the suspension, the measured of the ground motion is in good agreement with the measure provided by a standard accelerometer for seismic application. In particular, in the band $2 \div 20\,Hz$ the transfer function between the measure of the ground motion with an episensor and with the interferometer, is about 1. In the frequency band $f > 20\,Hz$ the effects of the air pressure fluctuation due to the air conditioners are present and this decreases the sensitivity of the instrument. We think that, shielding

the instrument from this noise, the sensitivity can increase.

Unfortunately, at the moment, we are not able to act behind the mass and so a force feedback prototype has not been tested. However an error signal measured with an interferometer device is available and we can use it to control the bottom mass of the suspension. In this way, locking the interferometer, for example, on the dark fringe, we can archive a measure of the ground displacement and, through the control signal, of the ground acceleration with a typical sensitivity of the interferometers (fraction of laser wavelength).

Future developments of this work involve:

- the project of a portable version of the sensor, shown in the chapter 2, to test it in site measurements;

- the implementations of an actuator system to control the bottom mass using the interferometer signal to test a force feedback prototype;

- the use of a ultra low frequency (ULF) suspension, shown in the paragraph 4.3, to reduce the resonant frequency of the pendolar system. In this way we can be able to measure ground acceleration in low frequency band ($f < 1\,Hz$).

Bibliography

[1] L. D. Landau and E. M. Lifshitz, *Theory of Elasticity*, Pergamon, Oxford, 1986.

[2] K. Aki and P. G. Richards, *Quantitative Seismology*, University Scientific Books, 2002.

[3] T. Lay and T.C. Wallace, *Modern global seismology*, Academic press, 1995.

[4] L.Andrews and R. Phillips, *Laser beam propagation through random media*, SPIE, 1998.

[5] K. Ishihara, *Soil Behavior in Earthquake Geotechnics*, Oxford Scinze Publications, Oxford, 1996.

[6] J. Berger and R. Lovberg, *Earth strain measurements with a laser interferometer*, Science, 170, 296-303, 1970.

[7] J. Levine and J.L. Hall, *Design and operation of a methane absorption stabilized laser strainmeter*, J. Geophys. Res. , 77, 2595-2609, 1972.

[8] N.R. Goulty, C.P. King and A.J. Wallard, Iodine stilized laser strainmeter Geophys. J. R. Astronom. Soc., 9, 269-282, 1974.

[9] S. Takemoto, *Laser interferometer systems for precise measurements of ground-strains*, Bull. Disaster Prev. Res. Inst. Kyoto Univ., 29, 65-81, 1979

[10] M.N. Dubrov and V.A. Alyoshin, Laser strainmeters: new developments and earthquake prediction applications, Tectonophysics, 202, 209-213, 1992

[11] L. Crescentini, A. Amoruso, G. Fiocco, G. Visconti, *Installation of a high-sensitivity laser strainmeter in a tunnel in central Italy*, Rev. Sci. Instrum., vol. 68, no. 8, pp. 3206-3210, Aug. 1997.

[12] A.Araya, K.Kawabe, T.Sato, N.Mio, K.Tsubono, *Highly sensitive wideband seismometer using a laser interferometer*, Rev. Sci. Instrum., 64 (5), 1993.

[13] Z.B. Zhou, Y.Y. Yi, S.C. Wu, J. Luo, *Low frequency seiswmic spectrum measured by a laser interferometer combined with a low frequency folded pendulum*, Meas. Sci. Technol., 15 (2004), 165-169.

[14] J. Liu, D.G. Blair, L. Ju, *Near-shore ocean wave measurement using a very low frequency folded pendulum*, Meas. Sci. Technol., 9 (1998), 1772-1776.

[15] M. Born and E. Wolf, *Principles of Optics*, Pergamon Press, Oxford, 1964.

[16] H. Barrel and J.E. Sears, *Phil Trans. Roy. Society*, A258, pp. 1-64, 1936.

[17] B. Edelin, *The Refractive Index of the air*, Metrologia, Vol.2, No.2, 71, 1966.

[18] F.Barone, R.De Rosa, L.Milano, K.Qipiani, *A Laser Interferometry Based Seismic Sensor*, 2002, in Proceedings of the 9th SPIE International Symposium on Remote Sensing for Environment Monitoring, GIS Application and Geology II, Manfred Ehlers Editor, vol.4886, 22-27 September, Crete, Greece, p.614-621.

[19] F.Acernese, F.Barone, R.De Rosa, L.Milano, K.Qipiani, *Michelson Interferometer System for Seismic Noise Measurement*, 2002, in Proceedings of the 10th SPIE International Symposium on Remote Sensing, 8-12 September, Barcelona, Spain (in press).

[20] F. Barone, E. Calloni, R. De Rosa, L. Di Fiore, F. Fusco, L. Milano, G. Russo, *Fringe Counting Technique used to Lock a Suspended Interferometer*, Applied Optics, Vol. 33, p. 1194, 1994.

[21] F. Barone, E. Calloni, L. Di Fiore, A. Grado, L. Milano, G. Russo, *Digital Error Signal Extraction Technique for Real-Time Automatic Control of Optical Interferometers*, Applied Optics, Vol. 34, p.8100-8105, 1994.

[22] *VIRGO proposal: Final conceptual design*, University of Pisa, Italy, unpublished.

Electronic Schemes
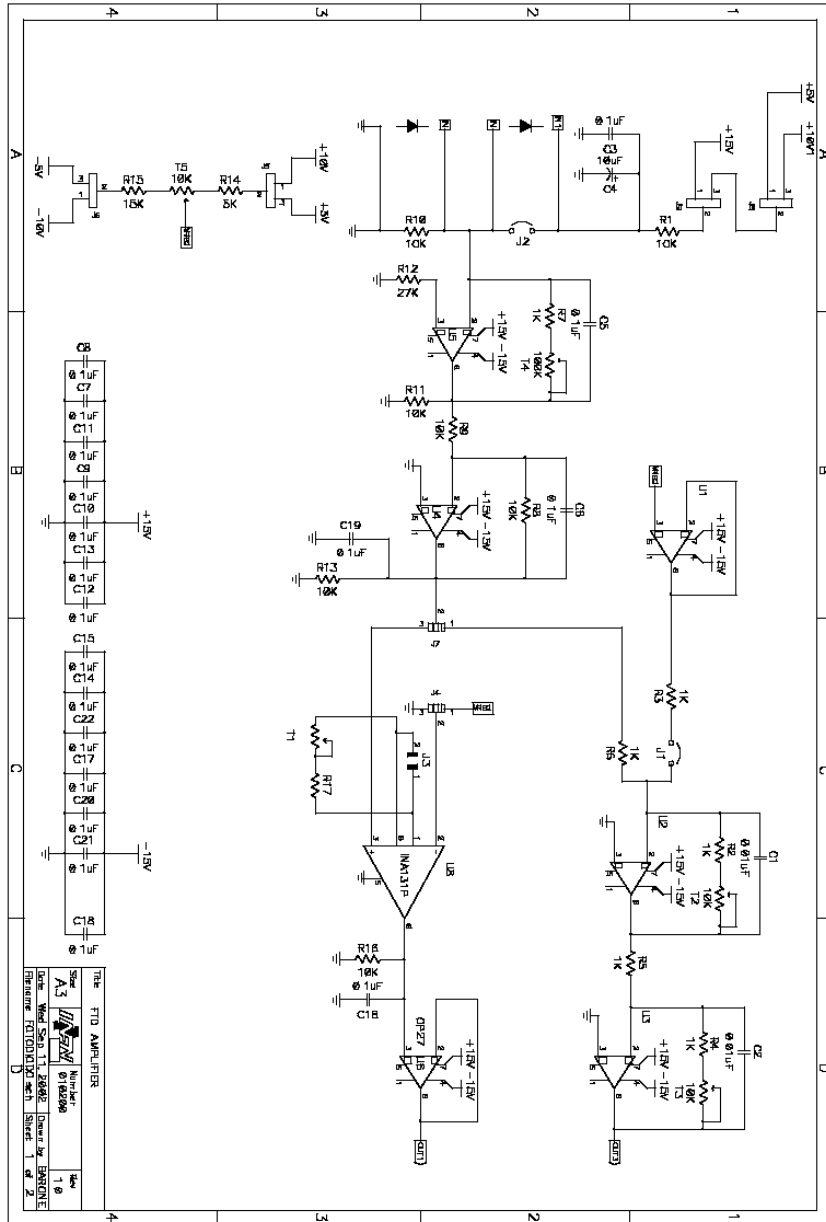
Figure 18: Amplifier of the photodiodes signal.
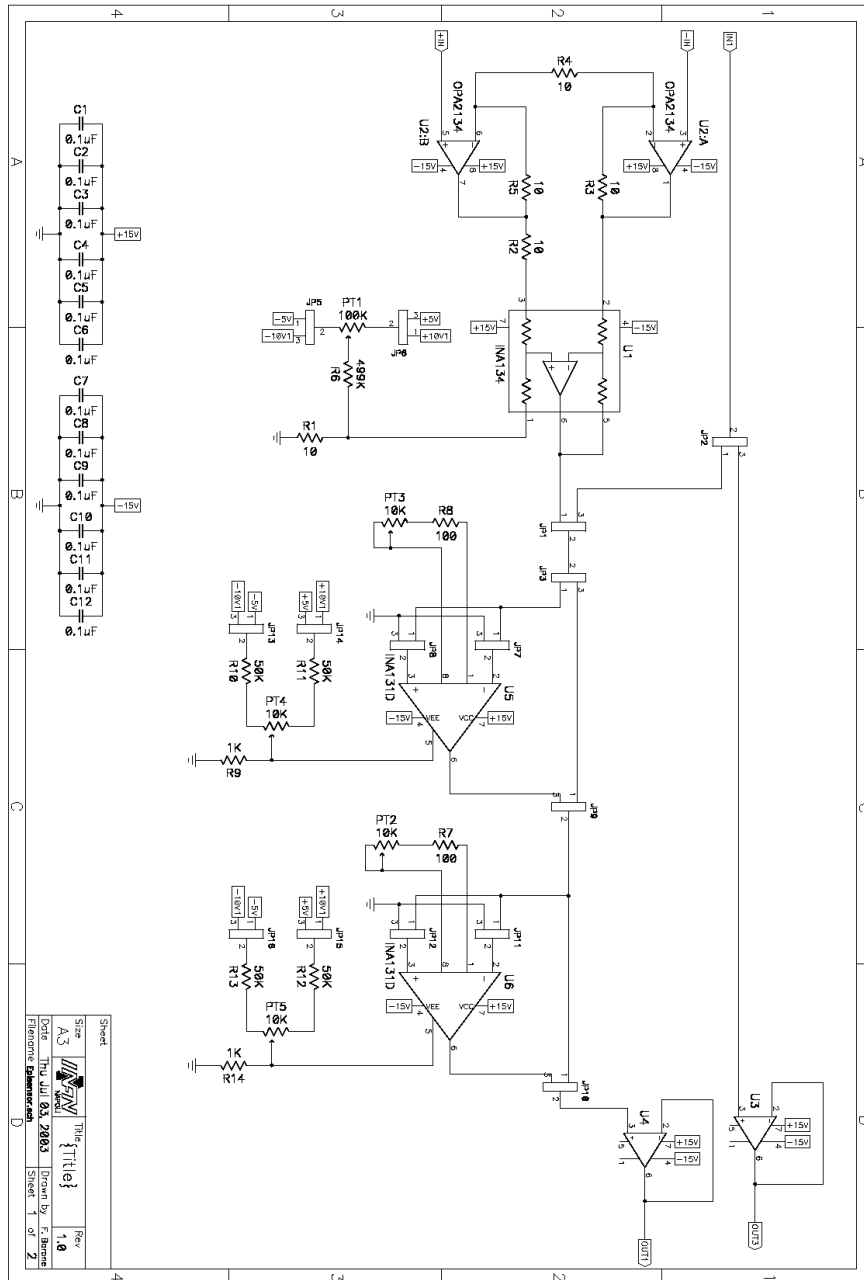
Figure 19: Amplifier of the episensor signals
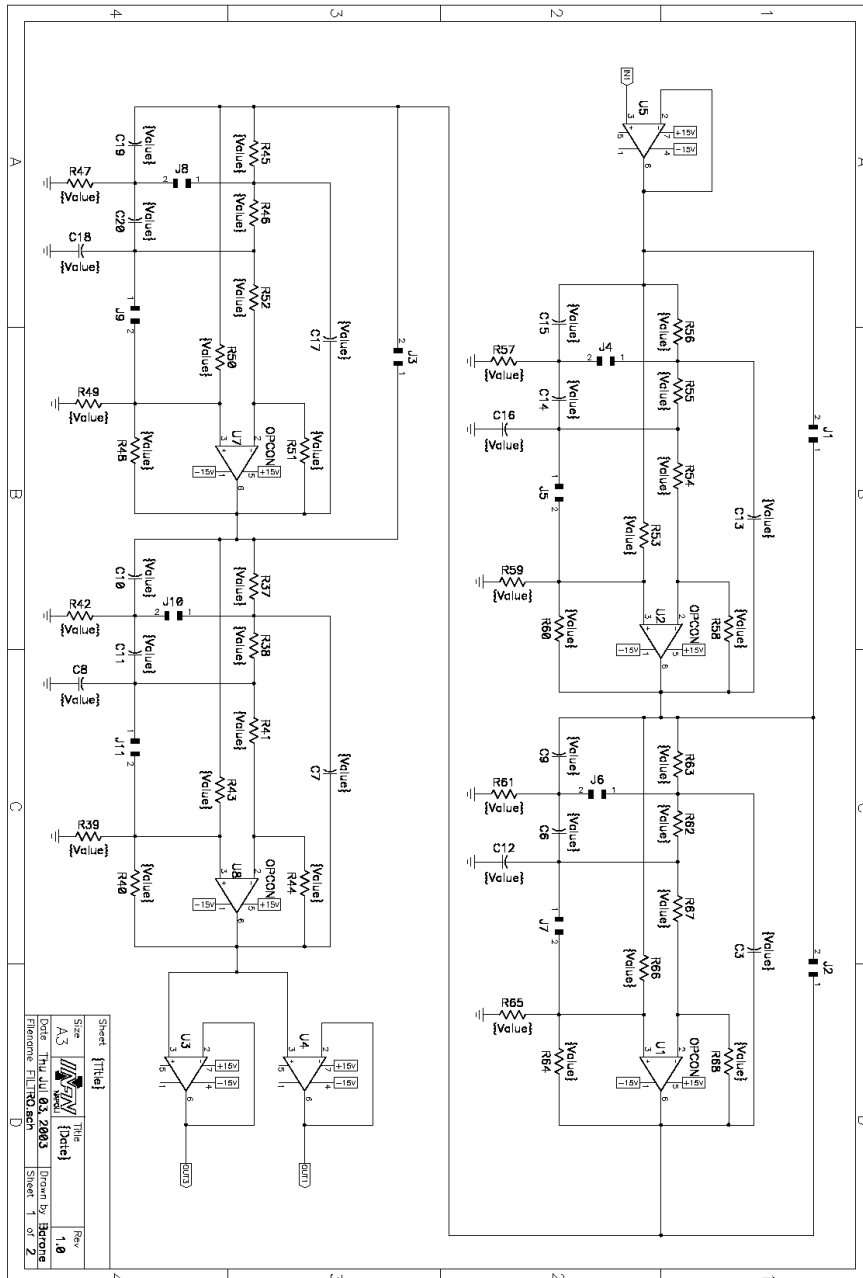
Figure 20: Antialiasing filters.

Central differences

Consider a function $f : [a, b] \rightarrow \Re$, continuous and with continuous derivative in $[a, b]$, and we want to approximate the first derivative in $\bar{x}$. Let $h > 0$ be a small real numerical value, the incremental

$$\delta_+ f(\bar{x}) = \frac{f(\bar{x} + h) - f(\bar{x})}{h} \tag{23}$$

can be considered an approximation of $f'(\bar{x})$. The error in this approximation can be calculated considering the expansion in Taylor series of $f(x)$ in $\bar{x}$. In fact

$$f(\bar{x} + h) = f(\bar{x}) + hf'(\bar{x}) + \frac{h^2}{2}f''(\xi) + o(h^3) \tag{24}$$

where ξ is a point in $(\bar{x}, \bar{x} + h)$. In this way the equation 23 becomes

$$\frac{f(\bar{x} + h) - f(\bar{x})}{h} = \delta_+ f(\bar{x}) = f'(\bar{x}) + \frac{h}{2}f''(\xi) + o(h^2) \tag{25}$$

and so approximating $f'(\bar{x})$ with $\delta_+ f(\bar{x})$ we make an error of $o(h)$. For this reason the approximation 25 is called *finite difference formula*. In the same way it is possible consider the Taylor series of $f(\bar{x})$ using back difference

$$f(\bar{x} - h) = f(\bar{x}) - hf'(\bar{x}) + \frac{h^2}{2}f''(\eta) + o(h^3) \tag{26}$$

where η is a point in $(\bar{x} - h, \bar{x})$.

Subtracting the equation 24 and 26 we obtain the approximation of the first derivative $f'(\bar{x})$ called *central difference*:

$$\delta f(\bar{x}) = \frac{f(\bar{x} + h) - f(\bar{x} - h)}{2h} \tag{27}$$

Using this approximation, we make an error of $o(h^2)$ instead of $o(h)$, as in the case of the forward or backward difference, which can be evaluate considering that

$$f'(\bar{x}) - \delta(\bar{x}) = \frac{h^2}{12}[f'''(\xi) - f'''(\eta)].$$ (28)

Ringraziamenti